Ion Photon Entanglement in a Parabolic Mirror Trap

Chen-Kuan Chou

A dissertation

submitted in partial fulfillment of the

requirements for the degree of

Doctor of Philosophy

University of Washington

2017

Reading Committee:

Boris Blinov, Chair

Kai-Mei Fu

Jens Gundlach

Program Authorized to Offer Degree:

Department of Physics

University of Washington

Abstract

Ion Photon Entanglement in a Parabolic Mirror Trap

Chen-Kuan Chou

Chair of the Supervisory Committee:
Associate Professor Boris Blinov
Department of Physics

Single trapped ion qubits are excellent candidates for quantum computation and information, and they also possess the ability to coherently couple to single photons. Efficient fluorescence collection is the most challenging part in remotely entangled ion qubit state generation. To address this issue, I developed an ion trap combining a reflective parabolic surface with trap electrodes. This parabolic trap design covers a solid angle of 2π steradians, and allows precise ion placement at the focus of parabola. I measured 39% fluorescence collection efficiency from a single ion with this mirror trap, and 10% single-mode optical fiber coupling efficiency out of the total reflected fluorescence. A deformable mirror was used to reduce aberration to less than 2.8 times over the diffraction limit. By analyzing the ion behavior in this RF quadrupole trap, I determined that the optical resolution is limited by ion micro-motion.

When trapping singly ionized barium, entanglement can be established between its energy level and the polarization of fluorescence. This setup generates an entangled ion-photon pair at 1 Hz with a mode-locked pulsed laser as the excitation source. Quantum correlation was measured between the ion spin state and the photon polarization state, and found to be above the 50% classical limit and the 71% threshold required for a Bell's inequality violation test.

TABLE OF CONTENTS

LIST OF FIGURES

LIST OF TABLES

ACKNOWLEDGEMENTS

First of all, I would like to thank Professor Boris Blinov for his continuing support. He always pointed me in the right direction when I was stuck in my research. I can't remember how many times I asked to take a day off because of my daughter, and he was always supportive. Secondly, I would like to thank my reading committee, Professor Kai-Mei Fu and Professor Jens Gundlach, for reviewing this thesis. The physics department people, including front desk officer, graduate advisor, and machine shop personnel, also helped me for a long time.

There are many students and post-docs who worked in Boris' group at different times, and I appreciate your company. Thank you to Richard Graham, Zichao Zhou, Tom Noel, John Wright, Matt Hoffman, Spencer Williams, Shaw-Pin Chen, Carolyn Auchter, Tomasz Sakrejda, and Jennifer Lilieholm. I would particularly like to thank Gang Shu, who started this project and shared his knowledge with me.

I would like to thank my parents; without them I wouldn't be here. Thanks to my two sisters for your company. I would particularly like to thank my mother-in-law, who helped me greatly during my PhD study. Most importantly, thank you to my wife, Wen-Yang, and my daughter, Claire, for being my family and bringing me joy in my life.

Chapter 1. BACKGROUND: QUANTUM COMPUTING AND BELL'S INEQUALITY

1.1 QUANTUM MECHANICS & BELL'S INEQUALITY

Quantum mechanics is one of the most precisely tested, and yet most argued about theories in physics history (*1*). One of its assumptions is entanglement between multiple physical states, where each individual state is bound to other states. Another important assumption is superposition, which means that the state of a physical system is undetermined, and can only be described as a sum of many quantum states. This superposition state will randomly jump into one of the probable state when somebody observes it. This counter-intuitive interpretation is clearly expressed in the Schrödinger's cat thought experiment: a cat, a radioactive atom, and a Geiger-counter-controlled poison are all sealed together in a box. When the Geiger counter detects radiations, it will release poison which kills the cat. Quantum mechanically, the state of the cat and the radioactive source is entangled, and the system state is a superposition between two possible situations:

$$|Alive\rangle_{cat}|Whole\rangle_{atom} + |Dead\rangle_{cat}|Decayed\rangle_{atom}, \quad (1.1)$$

and the time-dependent parameters are ignored here. At any given time, the cat is neither alive nor dead but is in a mixed state between the two, which is against the objective reality assumption in physics. It remains mixed until someone opens the box and makes an observation; then the state will collapse randomly into one of the eigenstates instantly, and the cat and the atom states are changed simultaneously. If we separate the cat and the atom apart first before our measurement, this simultaneous behavior in quantum mechanics will violate locality assumption

in Special Relativity of Albert Einstein (*2*). If quantum mechanics is correct, we must give up either the idea of locality or the idea of reality, if not both. The most well-known protest against quantum physics is the EPR paradox proposed by Einstein, Podolsky, and Rosen in 1935 (*3*). Although quantum mechanics had been verified in various experiments with very high accuracy, this counter-intuitive nature puzzled physicists for years. In 1964, John Bell finally proposed an inequality with measurable correlation parameters, which tests this instant interaction at a distance in quantum mechanics, namely quantum entanglement (*4*). The Bell's inequality test is very demanding in experiment design, because we are dealing with the idea of instant interaction, which is beyond the speed of light. Until recently, the complete Bell's inequality violation test finally carried out and quantum mechanics is strictly proved to be correct, which means that we are not living in a universe of both locality AND reality (*5*-*7*).

1.2 Quantum Algorithm & Computation

The very unusual nature of quantum mechanics has great potential to surpass their classical counterpart in many applications, like quantum cryptography and quantum computation (*8*). Quantum cryptography exploits the quantum phenomenon that measuring a physical state will change it. For example, in quantum information application, any eavesdropping action in data transfer can be detected at the cost of a fraction of data used as verification bits (*9*). It is due to the no-cloning theorem, which provides "unconditional security" theoretically, such that if Alice and Bob are sharing a quantum state, a third party Eve cannot intercept correct information in-between without being noticed (*10*).

Quantum computation utilizes superposition states, where the number of possible states can increase exponentially with the number of objects. For example, a spin state of 10 electrons system can be a superposition of $2^{10} = 1024$ different states, and it only takes several hundred quantum particles to generate a system that has more possible states than the number of atom in the whole universe. Several algorithms have been developed, and exploit this advantage to perform some kind of calculation through the interaction of these states, which outperforms the linear algorithms in classical computer on some applications, like factorization and database search (*11, 12*). It is still unclear whether we should replace all routine tasks that already execute perfectly in PC nowadays with quantum computer, but it is without the doubt that quantum computer can be of great help in some specialized fields, like quantum simulation of chemistry and cosmology (*13*). In the era that the famous Moore's law is no longer valid due to the difficulty of shrinking transistors further and further in nanometer scale, quantum computer is a potential solution to increase processing power of a central processing unit (CPU) (*14, 15*).

Without a doubt, quantum computing research is getting more and more popular in recent years, but it is also realistic to study the limitations of its capability. First, the logic behind quantum mechanics is very different from classical CPU. For example, AND, OR, NOT, and NAND gates are the basic logic gates in a modern CPU core, while Hadamard, controlled NOT, and rotation gates are considered as universal quantum gates in the qubits system (*8*). It may not be in the best interest to transform every classical algorithm into quantum logic, but there are some great examples proposed, like Shor' factoring algorithm and Grover's search algorithm (*11, 12*). Another common myth in quantum computing is its exponentially increasing processing power, a.k.a. parallel calculation. People in computer science categorize a problem into different groups by its complexity. The basic class is called the polynomial problem, which can be solved

by a classical computer (a.k.a. deterministic Turing machine) in a polynomial number of steps with best known algorithm (*16*). There is another class called the non-deterministic polynomial problem, which a classical computer can verify a given answer in polynomial number of steps to a question. There is the famous P=NP problem. Clearly, P problems are a subset of NP problems, but the opposite is not considered true, i.e. factorization of a big integer. It is believed that a quantum computer can only solve a fraction of NP problems efficiently in polynomial number of steps, which is categorized as the bounded-error quantum polynomial time class (BQP). Their relation is shown in Figure 1.1. Outside the NP problems is the PSPACE class, which is all problems that can be solved with a polynomial amount of memory (*17*).

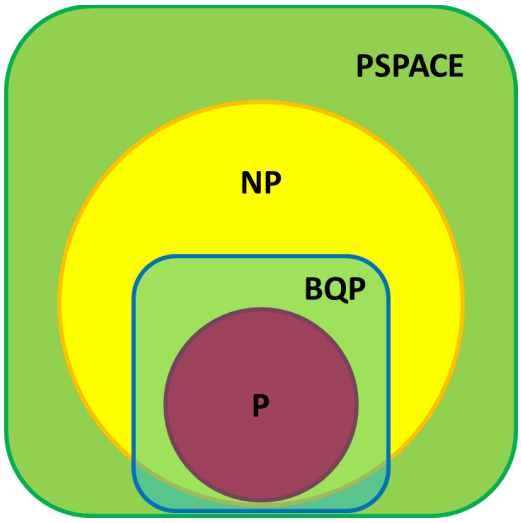

Figure 1.1. The complexity of computational problems is categorized into different classes by the number of steps required by a classical computer to solve it with best known algorithm. PSPACE includes problems that require a polynomial amount of memory to solve, NP stands for the non-deterministic polynomial problem, P stands for the polynomial problem, and BQP is the problem class that quantum computer can solve in polynomial number of steps.

1.3 Quantum Computer Architectures

The reliable generation of entanglement is the first crucial step for the realization of quantum computing and distant quantum communication. If the interaction between a quantum system and the environment is strong enough to reveal the information about the state, it becomes a measurement and changes the state randomly. Therefore, a quantum state is vulnerable to any environment perturbation. The entanglement state generation, transportation, manipulation, and detection are the basic operations in many quantum applications. Entanglement and the means for communication have been demonstrated recently in quantum dots (*18, 19*), nitrogen vacancy centers in diamond (*20, 21*), neutral atoms (*22*), atomic ensembles (*23*), superconducting qubits (*24*), and trapped ions (*25, 26*). In order to realize a quantum computer, there are several conditions called "DiVincenzo's criteria" that needs to be met (*27*):

1. Scalable quantum bit (qubit) system,
2. Initialization of qubit state,
3. Long coherence time,
4. Universal quantum gates, and
5. Qubit state measurement.

At the time of this thesis being written (Spring 2017), there are several candidate qubit systems that compete with each other as a building block of a first quantum computer. To name a few, there are superconducting qubits (*28*), trapped ions (*29*), silicon quantum dots (*30*), topological qubits (*31*), and diamond vacancies (*32*). Each candidate has its own advantages and disadvantages. Table 1 lists some promising candidates' progress up to date.

Table 1. Quantum computer progress chart of competing technologies developed in different companies (*33*).

Technology	Pros	Cons	Qubit longevity	Qubits entangled	Pursued by
Superconductors	Fast operation (ns scale)	Collapse fast, must keep cold	50 μs	9	Google, IBM
Trapped ions	Stable, highest gate fidelity	Slow operation (us scale), need many lasers	Hours	14	ionQ
Silicon quantum dots	Compatible with semiconductor industries	Only 2 qubits entangled, must keep cold	30 ms	2	Intel
Topological qubits	Low error rate	Not yet confirmed	N/A	N/A	Microsoft, Bell Labs
NV centers in diamond	Operate at room temperature	Difficult to entangle	10 s	6	Quantum Diamond Technologies

We choose the trapped ion system which meets all the requirements and is a promising candidate for quantum computer (*34*). In this thesis, the barium ion energy levels and photon polarizations are chosen as quantum states carriers. There are several advantages of this setup. First, the ion is trapped in free space in an ultra-high vacuum (UHV) system, which is well isolated from the environment perturbations, and the ion's energy levels are easily manipulated by lasers. Secondly, the photon is the best flying qubit for distant quantum communication. The ability to entangle and transport a photon allows us to construct a scalable network for quantum computing. A programmable five-qubits quantum computer has been demonstrated with trapped ions (*29*), and a Modular Universal Scalable Ion-trap Quantum Computer (MUSIQC) scheme is

proposed to realize a quantum computer as well (*35*). It utilizes the mobility of photon as a flying qubit to communicate between individual blocks that contains tens of trapped ions, and performs gate operation and information transmission. The main challenge in the ion-photon protocol is that the collection efficiency of the photon emitted from the trapped ion is very low, which slows down the entanglement generation and state readout efficiency. To address this problem, my thesis is aimed at increasing the solid angle coverage of a single trapped ion with a novel trap design.

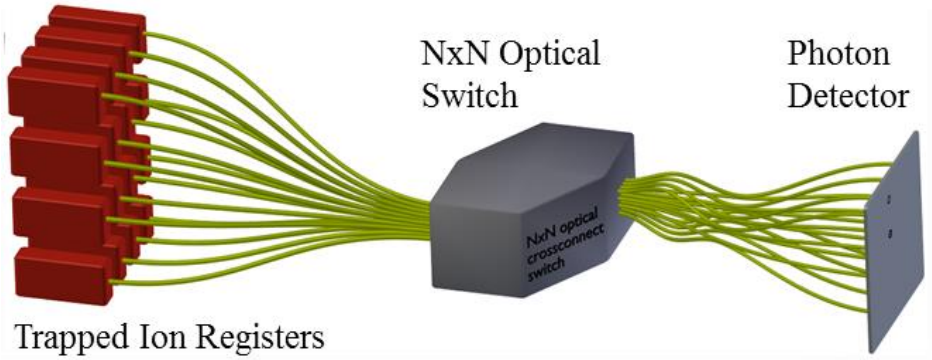

Figure 1.2. Modular Universal Scalable Ion-trap Quantum Computer proposal diagram (*35*). Ions are trapped in UHV systems and manipulated with lasers. Photons carry quantum information and cross-connect the ion qubits through optical fiber.

In this thesis, I report on a novel ion trap design which increases photon collection efficiency by 4 folds compared to traditional optical lens approaching. It can reliably generate ion-photon entanglement pair through optical fiber coupling, and their quantum correlation fidelity is determined above the classical limit and Bell's inequality test threshold. This system is well suited for quantum computation and communication propose, because the barium ion we use has energy spectrum of relatively long wavelength, making it suitable for long range fiber

optic transmission. With two identical setups, we can generate remote ion-ion entangled state through photon detection, and I also propose a Bell's inequality violation experiment, which is described at the end of the thesis.

Chapter 2. ATOMIC PHYSICS: BARIUM ION TRAPPING AND MANIPULATION

2.1 BARIUM ISOTOPES, IONIZATION, AND ENERGY STATES

The element I use in my experiment is barium, which is an alkaline earth metal. When it is singly ionized, its electronic configuration becomes hydrogen-like, which is simple and easily manipulated with lasers. There are many barium isotopes in nature, and Table 2 shows their relative abundance and some physical properties. We choose barium 138 because it is the most abundant isotope and has no nuclear spin, which simplifies the energy level diagram.

Table 2. Barium isotopes whose natural abundances are above 1%

Barium isotope	Nature abundance	Atomic mass (u)	Nuclear spin ($\hbar$)
^{134}Ba	2.4%	133.9	0
^{135}Ba	6.6%	134.9	3/2
^{136}Ba	7.9%	135.9	0
^{137}Ba	11.2%	136.9	3/2
^{138}Ba	71.7%	137.9	0

In order to trap barium ions, we need to spread barium atoms in space and ionize them. To begin with, a barium chunk is placed in a ceramic tube surrounded by tungsten wire loops, and heated by running high current through the wire. Barium atoms will evaporate toward the

center of the trap, where the ionization lasers are pointing. They are first excited from $6S_0$ state to $6P_1$ state by the 791 nm laser, and then ionized by the 337 nm laser. This two-stage excitation allows us to selectively ionize a single isotope by tuning the 791 nm laser frequency, which is shown in Figure 2.1. These two ionization laser beams are oriented at 90° to the barium atomic beam to reduce frequency shift due to the Doppler effect.

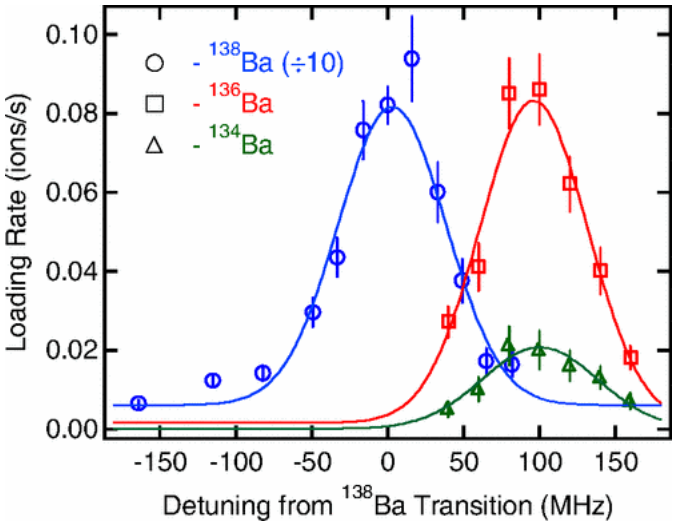

Figure 2.1. The loading rate of different barium isotopes vs. the 791 nm laser frequency detuning (*36*). The ^{138}Ba data is scaled by 1/10.

Figure 2.2 shows the basic barium ion levels used in this thesis: $6S_{1/2}$ is the ground state, $6P_{1/2}$ and $6P_{3/2}$ are the two excited states of lifetime around 10 ns, $5D_{3/2}$ is the long-lived metastable state involved in Doppler cooling cycle, and $5D_{5/2}$ is another long-lived metastable state, which the electron can be shelved into for qubit state readout.

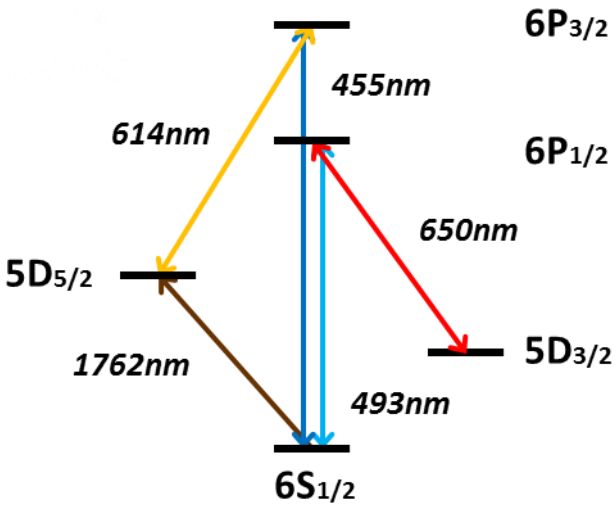

Figure 2.2. ^{138}Ba ion energy levels used in this thesis. $6P_{3/2}$ and $6P_{1/2}$ are of lifetime around 10 ns, and $5D_{5/2}$ and $5D_{3/2}$ are of lifetime over one minute due to the selection rule of angular momentum. In my experiment, I use the 650 nm and 493 nm transitions for Doppler cooling, 455 nm for entangled state initialization, and 1762/614 nm for qubit state detection/deshelving.

2.2 Ion Trapping

In order to use the barium ion as a qubit, we need to stabilize it in space, which requires a trapping potential in the form of $\Phi \propto r^2$. In classical electrodynamics, the sum of the second derivatives of the electric potential in three dimensions is zero in free space, which means that a charged particle cannot be confined by statics electric fields in all three directions simultaneously:

$$\frac{\partial^2 V}{\partial x^2} + \frac{\partial^2 V}{\partial y^2} + \frac{\partial^2 V}{\partial z^2} = 0. \tag{2.2}$$

Instead, we can create a pseudo potential by a dynamic electric field. In Figure 2.3, if we apply an oscillating voltage at radio frequency (RF) to the center ring electrode, the charged particle near the trap center will be driven back and forth in axial and radial directions

alternatively without escaping. Such a device is called the Paul Trap, one of the two ion trapping mechanisms that won the Physics Nobel Prize in 1989 (*37*).

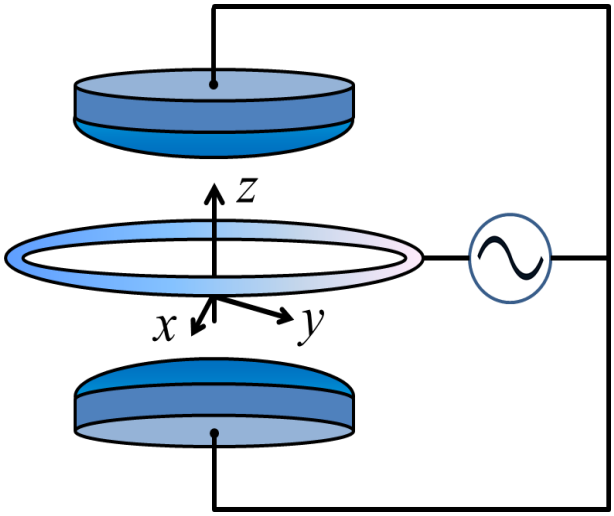

Figure 2.3. Classic Paul trap design consists of two grounded hyperbolic end-cap electrodes and a ring electrode connected to a RF oscillating signal.

As shown in Figure 2.3, a classic Paul trap consists of two grounded hyperbolic end-cap electrodes and one ring electrode oscillating at high RF potential. According to the Gauss law, the potential near the center of the trap can be written as

$$\Phi = (U + V\cos\omega t)(x^2 + y^2 - 2z^2), \tag{2.3}$$

where U and V are the potential constants and ω is the RF frequency. Solving this equation in x axis first, we have

$$F = m\frac{d^2x}{dt^2} = -e\frac{\partial V}{\partial x} = -2ex(U + V\cos\omega t), \tag{2.4}$$

which is in the form of the Mathieu equation, where m and e are the mass and charge of the charged particle (*38*). The behavior of equation of motion in x direction depends on two

dimensionless parameters, which are $a_x = 8eU/mR_0^2\omega^2$ and $q_x = -4eV/mR_0^2\omega^2$, where R_0 is the perpendicular distance of RF electrode to the trapping center in *x* direction. When $(|a_x|, q_x^2) \ll 1$, there is a steady state solution, which is

$$x(t) \approx \cos(\omega_x t + \phi)\,(1 + \tfrac{q_x}{2}\cos\omega t), \qquad (2.5)$$

where $\omega_x = \sqrt{a_x + q_x^2/2}\,\omega/2$ is called the secular frequency that corresponds to the pseudo potential in *x* direction (*39*). The typical one dimension trajectory as a function of time is shown in Figure 2.4. We can see that, along with the dominant oscillating motion at the secular frequency, there is a fast motion at the RF frequency, which is called the micro-motion. This is due to the RF oscillating fields which drive the charged particle when it is away from the center of pseudo potential. The amplitude of micro-motion in a typical Paul trap condition is usually an order of magnitude smaller than the amplitude of the secular frequency, and both can be reduced by laser cooling.

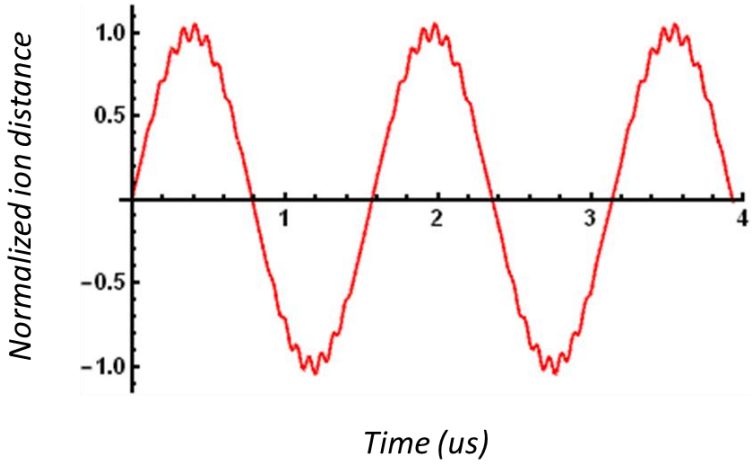

Figure 2.4. Trapped ion trajectory simulation in one dimension. The secular frequency is slower with larger amplitude, and the micro-motion frequency is faster with smaller amplitude. These parameters are set as $a = 0.01$, $q = 0.2$, and $\omega = 12$ MHz.

2.3 DOPPLER COOLING

When the ion is first trapped, its kinetic energy may be as high as several hundred kelvin depending on the trapping potential, and will increase with time due to environment perturbations. In order to reliably observe and study the trapped ion, we need to constantly reduce its kinetic energy and minimize its position uncertainty. The Doppler cooling is the standard laser technique for this purpose (*40*). In quantum mechanics, atoms or ions only absorb photons at certain frequencies, which correspond to quantized electron energy levels. Due to the Doppler effect, when an ion moves toward a photon, the photon frequency is higher in the ion's reference frame than in the laboratory's frame. If we lower the laser frequency (red detune) from the ion's absorption spectrum, the ion is more likely to absorb photons that counter propagate toward it rather than those who travel in the same direction. Assuming an ion is moving with velocity *v*, its resonant absorption frequency is ω, and the laser frequency is ω_0, the photon scattering rate can be derived as:

$$R_{sc} = \frac{\Gamma}{2}\frac{\Omega^2/2}{\delta^2+\Omega^2/2+\Gamma^2/4}, \tag{2.6}$$

where $\Gamma = 1/\tau$ is the natural linewidth (one over lifetime), $\Omega = e\left\langle 0\middle|\vec{r}\cdot\overrightarrow{E_0}\middle|1\right\rangle/\hbar$ is the Rabi frequency determined by electric dipole moment and the laser strength, and $\delta = \omega - \omega_0 + kv$ is the photon frequency shift from resonance. Each photon has a momentum of $\hbar k$, where *k* is the wave number, and the scattering force $F_{sc} = \hbar k R_{sc}$. We can calculate the net force by summing F_{sc} of photons traveling in both directions:

$$F_{net} = F_{sc}(\omega - \omega_0 - kv) + F_{sc}(\omega - \omega_0 + kv). \tag{2.7}$$

At low ion velocity limit where $kv \ll \Gamma$, we will have

$$F_{net} \cong -2\frac{\partial F}{\partial \omega}kv = 16\hbar k^2 v\frac{\delta^3\Gamma}{(\Gamma^2+4\delta^2)^2}, \quad (2.8)$$

and we can define the laser cooling power as $dE_k/dt = vF_{net} = -\alpha v^2$, where $\alpha = -16\hbar k^2\delta^3\Gamma/(\Gamma^2 + 4\delta^2)^2$ is the damping coefficient and $\delta < 0$ for red detuning of laser frequency.

In addition to the cooling power of Doppler effect, each spontaneous emission photon will kick the ion in random direction. These recoils heat the ion and the heating power is calculated by random walk analysis. Assuming $v = 0$ at $t = 0$, in momentum space, we have the mean square momentum equal to squared momentum times the number of steps, which leads to $\overline{v_{x,y,z}^2} = v^2 R_{sc}t/3$ along any axis of Cartesian coordination at any given time. The heating power is thus $Md\overline{v_{x,y,z}^2}/2dt = 4Mv^2R_{sc}/3$, where M is the mass of atom. Equating the cooling and heating power, we obtain the kinetic energy at equilibrium in a given axis as $M\overline{v_z^2} = \hbar\Gamma/4$, which is known as the Doppler cooling limit. In our system setup, we use the $6P_{1/2}$ level as the Doppler cooling state, and the temperature we can achieve is about 2 mK ($\Gamma \approx 125$ MHz and $M = 138$ amu). This temperature is more than an order of magnitude higher than the ground state energy in our RF pseudo potential.

2.4 RABI OSCILLATION

In this section, I want to discuss the population transfer in a two-state system using the semi-classical approach, because it is related to the ion state shelving and readout purposes in my experiment. Assuming we have a system with non-degenerate energy states $|0\rangle$ and $|1\rangle$, whose energy is E_0 and E_1 respectively, its general wave function in Heisenberg picture can be written as a superposition state (*41*)

$$|\psi(t)\rangle = c_0(t)e^{-iE_0t/\hbar}|0\rangle + c_1(t)e^{-iE_1t/\hbar}|1\rangle, \quad (2.9)$$

where $c_{0,1}(t)$ are the square root of probability amplitudes of finding the system in states $|0\rangle$ and $|1\rangle$ at time *t* respectively, and $|c_0|^2 + |c_1|^2 = 1$. If we apply a potential $V(t) < H_0$, we can adapt the time-dependent perturbation theory which leads to

$$i\hbar\begin{bmatrix}\dot{c_0}\\ \dot{c_1}\end{bmatrix} = \begin{bmatrix}V_{00} & V_{01}e^{-i\omega_{10}t}\\ V_{10}e^{i\omega_{10}t} & V_{11}\end{bmatrix}\begin{bmatrix}c_0\\ c_1\end{bmatrix}, \quad (2.10)$$

where $\omega_{10} = (E_1 - E_0)/\hbar$. For an oscillating potential like electromagnetic wave, $V_{00} = V_{11} = 0$ and $V_{01} = V_{10}^* = \gamma e^{i\omega t}$, where γ is a strength constant and ω is the potential oscillating frequency. Assuming the wave function starts off with state $|0\rangle$, meaning that $c_0(0) = 1$ and $c_1(0) = 0$, we can solve the two coupled differential equations in Eq. 2.10 and obtain the solution as:

$$|c_1(t)|^2 = \frac{\Omega^2}{\mathrm{W}^2}\sin^2(\frac{\mathrm{W}t}{2}) \text{ and } |c_0(t)|^2 = 1 - |c_1(t)|^2, \quad (2.11)$$

where $W^2 = \Omega^2 + (\omega - \omega_{10})^2$. Equation 2.11 is the probability of two states as functions of time when the oscillating potential is applied, provided that the life time of both states are much longer than $1/\Omega$, so no spontaneous decay is occurred. Probability of finding the system in state $|1\rangle$ is oscillating with the amplitude related to the detuning between external potential frequency ω and resonant frequency ω_{10}. When ω is at the resonant frequency, the population inversion occurs and $|c_1(t)|^2 = 1$ at $t = \pi/\Omega$, which is called the π pulse. The ion's wave function will oscillate as a function of $\sin^2(\frac{\Omega t}{2})$. Figure 2.5 shows the maximum probability of finding the ion in state $|1\rangle$ at different frequency detuning. This phenomenon can be observed when the linewidth of both states are much longer than the Rabi frequency.

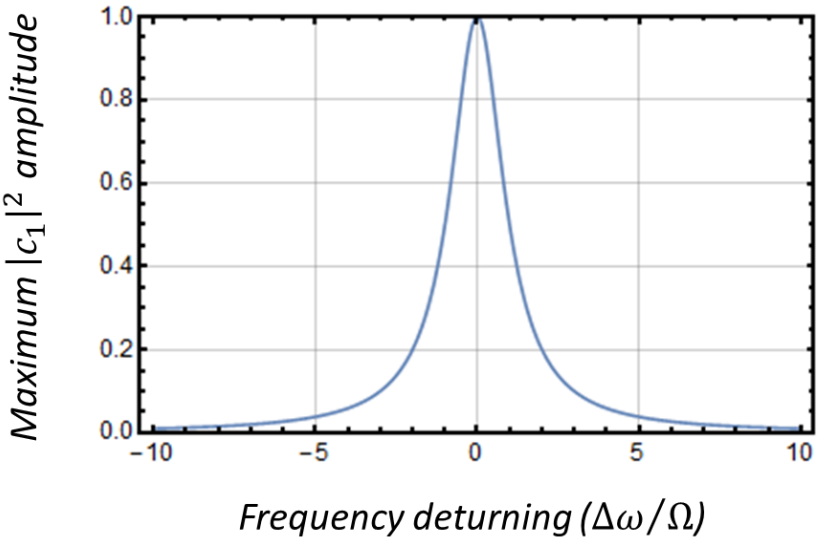

Figure 2.5. Maximum $|c_1|^2$ amplitude as the function of frequency detuning ($\Delta\omega = \omega - \omega_{10}$). The population inversion between two states can be achieved when the applied field is at resonant frequency.

2.5 Barium Cooling, State Initialization, Rotation, and Readout

At the end of this chapter, I would like to introduce some common techniques which manipulate barium ion. First, the basic barium ion cooling cycle consists of $6P_{1/2}$, $5D_{3/2}$, and $6S_{1/2}$ states in Figure 2.2. The branching ratio of $5D_{3/2}$ and $6S_{1/2}$ from $6P_{1/2}$ decay paths is roughly 1:3 (*42*). The Doppler cooling is performed by shining the 493 nm and 650 nm laser beams onto the trapped ion. By applying some external magnetic field, the Zeeman effect shifts electron energy levels by different spin orientations and the magnetic field strength, as shown in Figure 2.6. The polarization of the emitted photon between different transitions is determined by angular momentum conservation of the quantization axis, which is defined by the external magnetic field direction. The π polarized photon carries no angular momentum, while σ^+ (σ^-) polarized

photon carries angular momentum of +1 (–1) along the principle axis. In order to drive all possible transitions in the cooling cycle, the 493 nm laser cannot be only of σ^+ or σ^- polarizations, and the 650 nm laser should include both σ^+ and σ^- polarizations, which are defined by the direction of magnetic field. The spontaneous decay is a random process by quantum mechanics, which generates quantum entanglement between ion and photon. In this thesis, I use the $6S_{1/2}$ ground state splitting levels as qubit states $|0\rangle$ and $|1\rangle$, which are entangled to the photon polarization states.

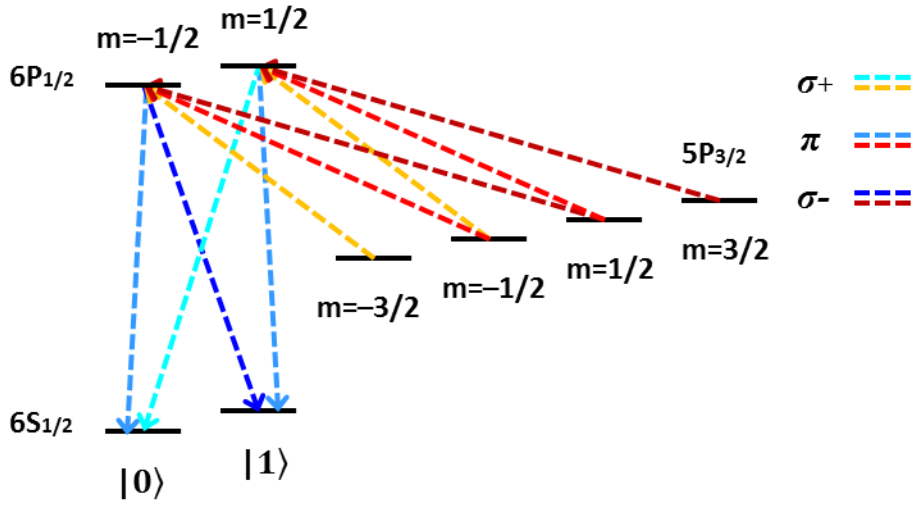

Figure 2.6. Basic barium ion cooling cycle and the energy splitting when an external magnetic field is applied. The selection rules demand that angular momentum changes in dipole transition can only be ±1 or 0, which is represented by different colors.

We can initialize the ion into a specific qubit state, either $|0\rangle$ or $|1\rangle$, by exploiting these selection rules. If we drive all $6S_{1/2}$ and $5P_{3/2}$ transitions in Figure 2.6 but one, the ion will eventually fall into the ground state of that transition after enough cycling. For example, when the 493 nm laser is of σ^+ (σ^-) polarization only, and the 650 nm laser is of both σ^+ and σ^-

polarizations, the ion will end up with the spin up (down) state of $6S_{1/2}$ with unity probability. This technique is called the optical pumping, and is often used in atomic systems for state initialization. The fidelity of state initialization is determined by the number of transition cycles and the laser polarization accuracy.

Next ion state operation is ion qubit rotation, which is a Rabi oscillation application. To test Bell's inequality violation, we need to measure the ion state in different bases. This is done by performing ion qubit state rotation followed by a qubit state readout operation. We can use Rabi oscillation between the two ion qubit states by applying oscillating electromagnetic field from outside the vacuum chamber. For example, the ion state can be rotated by 90° with a π/2 pulse at resonant frequency. In order to generate a strong RF electromagnetic field at ~10 MHz, which is the typical ion qubit states splitting, one can use a wire coil with a few tens of turns and an amplified sinusoidal signal as input. The power of RF radiation is maximized by matching the impedances of wire coil and the signal amplifier. A common practice of matching an arbitrary impedance in a given signal frequency requires two variable capacitors, one connected in parallel and one connected in series, as shown in Figure 2.7 (*43*). One can use the Smith chart, or calculate analytically to obtain the approximate values of the two capacitors. In our case, the signal amplifier has an input impedance $Z_{in} = 50$ ohm. Assuming the wire loop has impedance of $j\omega L + r$, where ω is the signal frequency, and L and r are the characteristic parameters of the coil, the values of the two matching capacitors can be approximated as $C_1 \approx \sqrt{r/Z_{in}}/\omega^2 L$ and $C_2 \approx (1 - \sqrt{r/Z_{in}})/\omega^2 L$.

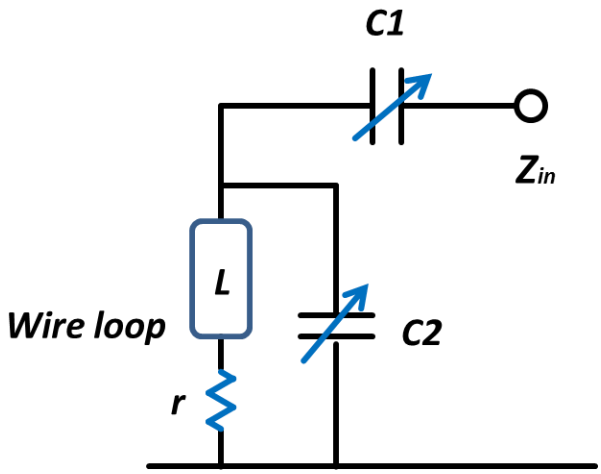

Figure 2.7. A simple impedance matching circuit with two variable capacitors, C_1 and C_2. The blue component is our RF electricmagnetic field generating coil. Input is connected to a singal amplifier, whose $Z_{in} = 50$ ohm.

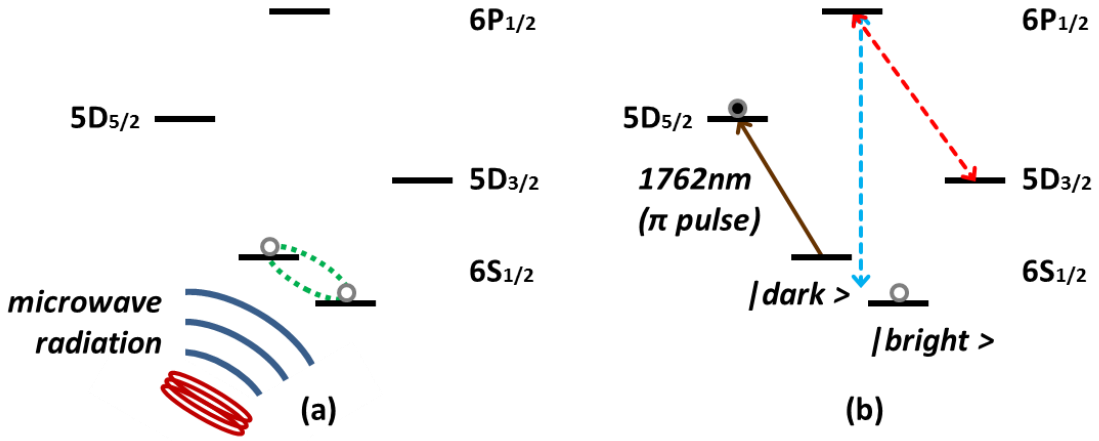

Figure 2.8. Barium ion qubit state rotation and state readout scheme. (a) Qubit states can be rotated by the means of Rabi oscillation. With 1 Gauss external magnetic field, the resonant frequency of splitted ground states is about 7 MHz. (b) By appling a π pulse of the 1762 nm laser, the ion in a particular ground state is shelved into the long-live $5D_{5/2}$ state. State readout is achieved with following cooling cycle and fluorescence detection with a PMT.

The final operation is the qubit state readout. By applying external magnetic field around 1 Gauss, the Rabi frequency of qubit states $|0\rangle$ and $|1\rangle$ is about 7 MHz. In order to read the ion qubit state, we shelve one of the states to $5D_{5/2}$ with the 1762 nm laser, followed by regular cooling cycle. The separation of absorption lines of two qubit states to $5D_{5/2}$ transitions is larger than our 1762 nm fiber laser's bandwidth, so we can shelve a particular ion qubit state by setting the 1762 nm laser to the resonant frequency. Because $5D_{5/2}$ state has lifetime around 30 seconds, the qubit being shelved is removed from the cooling cycle, thus we call it the "dark state". If the ion is in the other qubit state, it is not shelved and will go through cooling cycle with the 493 nm and 650 nm lasers, and we call it the "bright state". The state rotation and readout diagrams are shown in Figure 2.8. In our system, 95% state transfer from $6S_{1/2}$ to $5D_{5/2}$ with a π pulse is achieved. Figure 2.9 shows the histogram of PMT photon counts of 50 ms windows of dark and bright state events. The 37 counts can be used as the threshold to distinguish them.

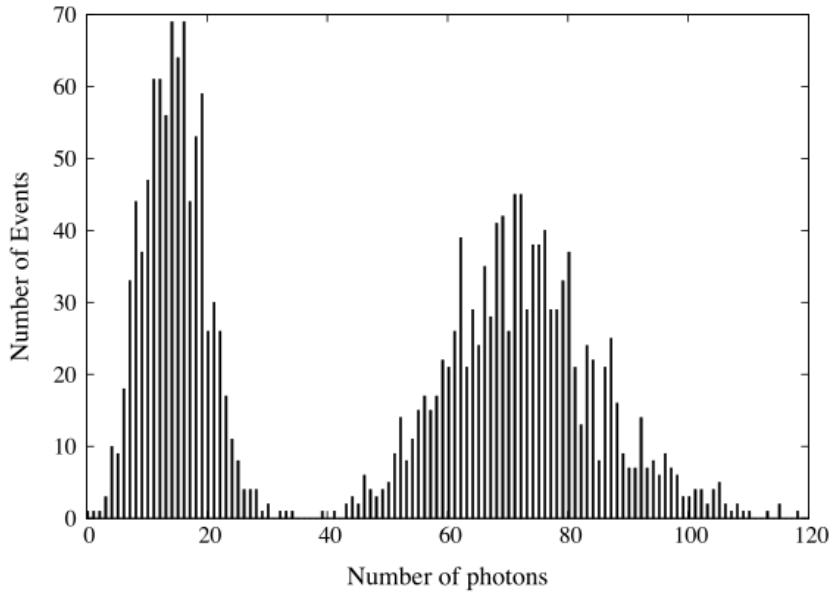

Figure 2.9. Histogram of PMT photon counts of several thousand dark and bright state events. The left peak corresponds to the dark state and the right peak to the bright state. By placing threshold of 37 photon counts, the singal to noise ratio is good enough to distinghish these two states.

Chapter 3. BELL'S INEQUALITY AND ION-PHOTON ENTANGLEMENT

3.1 BELL'S INEQUALITY & CSHS EQUATION

Entanglement is one of the most counter-intuitive ideas in quantum mechanics. If two or more particles are entangled, their individual states are bounded to each other (think of Schrodinger's cat) until an observation is made. Every entangled particle state is changed simultaneously by a single measurement. In the above statement, quantum mechanics challenges two casual concepts at once: reality and locality. Reality means that the physical state of anything is objective and exists at all time, regardless at whether people are watching it or not. Locality means that nothing including information can transmit faster than the speed of light, which is also known as casualty. These two ideas are hard to dispose at, and physicists have debated it for decades, because people didn't know how to test them. Einstein, Podolsky, and Rosen called quantum mechanics an incomplete theory because its probability nature fails to explain any measurement result (*3*). It wasn't until 1964 that John Bell proposed an inequality with a measureable quantity, which holds true in all local and realistic theories but is violated in quantum mechanics, which is non-local and/or non-realistic (*4*). In 1969, a modified version of the Bell's inequality, called the CHSH inequality was derived with correlation parameters, which is more accessible and has been implemented in various experiments (*44*). I am going to discuss its detail below.

To begin with, I use an entangled spin state of two electrons as an example:

$$|\psi\rangle = (|\uparrow\rangle_{z1}|\downarrow\rangle_{z2} - |\downarrow\rangle_{z1}|\uparrow\rangle_{z2})/\sqrt{2}. \tag{3.12}$$

In this quantum state, each electron has its own spin of $\hbar/2$ while the total spin is zero, and their z components are opposite to each other in this superposition state. Assuming I separate them apart but keep the entanglement, I can measure their spin states individually by setting two separate Stern-Gerlach experiments (*45*). I am free to choose the basis for every measurement, described by angles θ_1 and θ_2, and the result is assigned as $|1\rangle$ for spin up and $|0\rangle$ for spin down along the measurement direction I use. I can define the correlation parameters as a function of spin measurement results between two electrons:

$$P(\theta_1, \theta_2) = f_{11}(\theta_1, \theta_2) + f_{00}(\theta_1, \theta_2) - f_{10}(\theta_1, \theta_2) - f_{01}(\theta_1, \theta_2). \quad (3.13)$$

$f_{10}(\theta_1, \theta_2)$ is the probability of the events which electron 1 is spin up and electron 2 is spin down, where θ_1 and θ_2 are the angle of the spin measurement for electron 1 and 2, and *vice versa*. $P(\theta_1, \theta_2)$ can be regarded as correlated probability minus anti-correlated probability. In classical physics, the spins of both electrons are independent from each other. Therefore, the correlation parameters can be written as

$$P(a, b) = \int \bar{A}(a, \lambda)\bar{B}(b, \lambda)\rho(\lambda)d\lambda, \quad (3.14)$$

where $\bar{A}(a, \lambda)$ is the expectation value of electron 1 spin measurement, $\bar{B}(b, \lambda)$ is the expectation value of electron 2 spin measurement, λ is any hidden variable that may exists, and $\rho(\lambda)$ is the population distribution such that $\int \rho(\lambda) = 1$. The following equation derivation is based on John Bell's 1987 publication (*46*):

$$P(a, b) - P(a, b') = \int [\bar{A}(a, \lambda)\bar{B}(b, \lambda) - \bar{A}(a, \lambda)\bar{B}(b', \lambda)]\rho(\lambda)d\lambda, \quad (3.15)$$

then taking the absolute value on both sides and applying the triangle inequality, we get

$$|P(a, b) - P(a, b')| \leq$$
$$|\int \bar{A}(a, \lambda)\bar{B}(b, \lambda)[1 \pm \bar{A}(a', \lambda)\bar{B}(b', \lambda)]\rho(\lambda)d\lambda| +$$

$$|\int \bar{A}(a,\lambda)\bar{B}(b',\lambda)[1 \pm \bar{A}(a',\lambda)\bar{B}(b,\lambda)]\rho(\lambda)d\lambda|. \quad (3.16)$$

Because the values inside the brackets are non-negative, the right-hand-side becomes

$$|P(a,b) - P(a,b')| \leq 2 \pm \left[\iint \bar{A}(a',\lambda)\bar{B}(b',\lambda)\rho(\lambda)d\lambda + \int \bar{A}(a',\lambda)\bar{B}(b,\lambda)\rho(\lambda)d\lambda\right]$$
$$= 2 \pm [P(a',b') + P(a',b)]. \quad (3.17)$$

Applying the triangle inequality again, we can obtain

$$|S| = |P(a,b) - P(a,b') + P(a',b') + P(a',b)| \leq 2, \quad (3.18)$$

which is the CHSH inequality, and the upper limit of the quantity $|S|$ is 2 in classic physics. In quantum mechanics, taking the two electron spin system for example, the spin correlation function $P(a,b)$ of two electrons in Eq. 3.12 state measured at angle a and b is $-\cos(a-b)$. Then the CHSH inequality becomes:

$$S = |-\cos(a-b) + \cos(a-b') - \cos(a'-b') - \cos(a'-b)|, \quad (3.19)$$

for the entangled state in Eq. 3.12. Assuming I choose an orthogonal basis $(a,a') = (0,\pi/2)$ for electron 1 spin measurement, it can be seen that the strongest violation of CHSH inequality happens when electron 2 spin is measured at $(b,b') = (\pi/4\,, 3\pi/4)$ basis, for which $S = 2\sqrt{2}$~2.83 (*44*).

Since Bell's inequality has been published, there are many experiments trying to test it (*47-49*). Until recently, all Bell's inequality tests are subjected to at least one of two main loopholes, which are locality loophole and detection loophole (*5*). Locality loophole means that the detection events between entangled pair should be made in a space-like interval, such that no information is allowed to transform between them by Special Relativity. Detection loophole, or so-called the fair-sampling loophole, requires that the detection efficiency must be larger than $2/(\sqrt{2}+1) \approx 83\%$, such that the inequality is still violated even if all non-detected events are

anti-correlated (*50*). To overcome the locality loophole, we need to separate two entangled objects far enough while keeping the entanglement. Most locality loophole-free experiments use photon to fulfill the requirement, but single photon detection efficiency in modern device is much less than 83%, which subjects to the detection loophole. As the result, closing both loopholes puzzles physicists for many years.

3.2 Ion-Photon Entanglement Methods

We choose ion-photon system for our quantum entanglement experiments because of ion's stability and photon's mobility (*51, 52*). Photon is popular for its variety of qubit types and corresponding entanglement protocols, such as polarization (*53*), frequency (*54*), and time-bin protocols (*55, 56*). I am going to briefly discuss these in a trapped ion system, and move to my research design, which uses photon polarization and ion energy level as qubit states.

1. Frequency Qubit

Photon frequency is a constant when being transmitted in different media, thus it is not subjected to most environment perturbations. A general photon frequency qubit in an ion-photon system utilities two ground states and two excited states of ion energy levels shown in Figure 3.1a. Assuming we initialize the ion in a superposition $(c_1|\downarrow\rangle - c_2|\uparrow\rangle)$ in the ground state, we can use a laser pulse to drive a single transition of different resonant frequencies, provided that the laser's bandwidth is broad enough to cover both transitions. If, by selection rules, the only transitions allowed are of different resonant frequencies, then the ion will decay back with its state entangled to the photon frequency:

$$|\psi\rangle = c_1|\downarrow\rangle|\mathrm{b}\rangle - c_2|\uparrow\rangle|\mathrm{r}\rangle, \tag{3.20}$$

where $|\mathrm{b}\rangle$ and $|\mathrm{r}\rangle$ are denoted to blue and red photon states, respectively. In order to resolve the frequency qubit, their frequency shift should be larger than their transition linewidths.

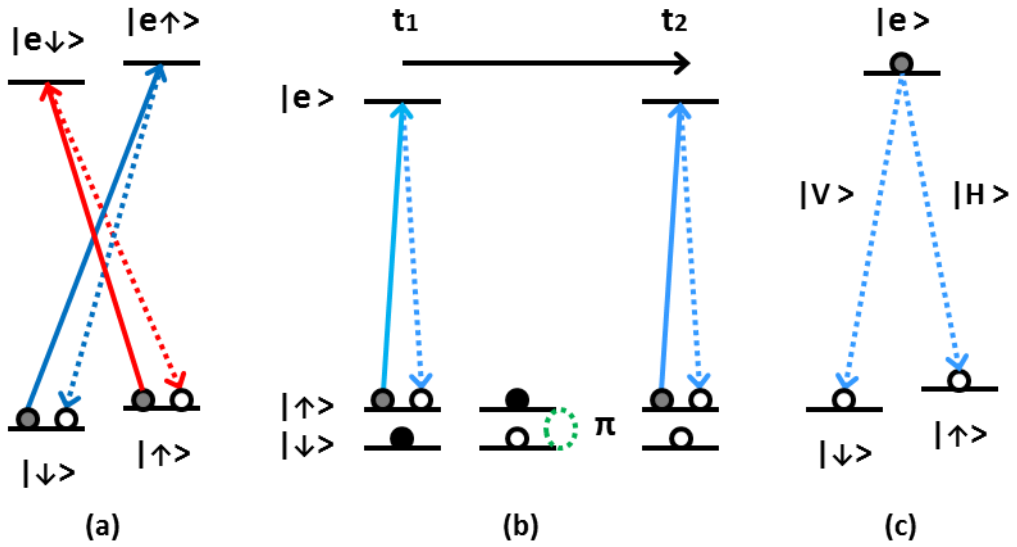

Figure 3.1. Different entanglement schemes for ion-photon system. The solid arrows represent laser excitation pulses, and the dashed lines represent photon emissions. (a) Frequency qubit: quantum information is stored in different frequencies due to ground and excited states splitting. (b) Time-bin qubit: the information is stored in the time frame when a photon is generated. (c) Polarization qubit: the information is stored in the angular momentum of the photon.

2. Time-bin Qubit

In additional to photon's physical quantity, we can use the timing information when a photon is generated as the qubit carrier. Starting with an ion in a superposition state of Eq. 3.12, we only need one excited state and two ground states, provided that only $|\uparrow\rangle \leftrightarrow |\mathrm{e}\rangle$ transition is allowed by selection rules. In such a case, shown in Figure 3.1b, we apply a single laser pulse to

drive this transition, followed by the ground state π rotation operation, then send another excitation laser pulse. The resulting ion-photon state will be:

$$|\psi\rangle = c_1|\downarrow\rangle|t_2\rangle - c_2|\uparrow\rangle|t_1\rangle, \tag{3.21}$$

and $|t_1\rangle$ and $|t_2\rangle$ are the timestamps when the photon is generated. These photon states can be resolved by Michelson interferometer setup with controllable optical path length.

3. Polarization Qubit

Due to angular momentum conservation, different transitions in atoms radiate photons of different polarizations. As shown in Figure 3.1c, the ion energy level can be entangled to photon polarization with a single laser excitation pulse, where an initial superposition ion state is not necessary. The resulting entangled state will look like:

$$|\psi\rangle = c_1|\downarrow\rangle|\mathrm{V}\rangle - c_2|\uparrow\rangle|\mathrm{H}\rangle, \tag{3.22}$$

where $|\mathrm{V}\rangle$ and $|\mathrm{H}\rangle$ are designated for vertical and horizontal polarization states. In order to extract the quantum information, the orthogonal polarization states are required. I used polarization qubit as my ion-photon entanglement protocol, because it is easier to realize in singly ionized barium's energy levels.

Chapter 4. EXPERIMENT I: NOVEL ION TRAP

4.1 PARABOLIC MIRROR TRAP

The original radiofrequency quadrupole ion trap designed by Wolfgang Paul is formed by one ring and two end-cap electrodes of hyperbolic shape, as illustrated in Figure 4.1 (*37*). Since its invention, there are various ion trap designs, including the most popular linear trap (*57*), fiber tip stylus trap (*58*), cavity trap (*59*), and the semiconductor chip trap (*60*). In our group, we developed the concept, and implemented the reflective surface trap (*61*). Its basic structure is derived from the original Paul trap. The Paul trap can be simplified to a ring plus two needles. The ring electrode can be further deformed into a rotationally symmetric optical surface with a hole at the center for one of the needles to pass through. If we keep one needle electrode, the strong field around its tip will define the trapping position. The other needle can be replaced by a ring to provide more optical access. Ions can be trapped on the axis of symmetry and moved following the translational movement of needle electrode. The trapping potential in the center is almost independent of the optical surface shape, which makes this design universal for different reflector profiles.

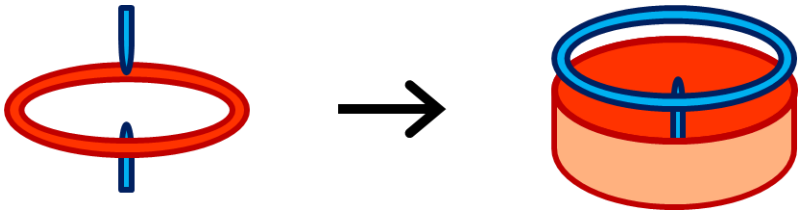

Figure 4.1. Paul trap morphing into a reflective surface trap. Blue electrodes are grounded and red electrode is at an RF potential, which reflects the ion fluorescence. The top needle electrode is replaced by a ring for optical access. The pseudo potential stays in the quadrupole form around the center of trap.

To improve optical performance of our previous spherical mirror trap (*61*), I built a trap with optical reflective surface in parabolic shape. By trapping an ion in the focus of parabola, it is designed to cover a half of the full 4π solid angle surrounding the ion, and collimate the reflected photons, which can transport quantum information in free space or through an optical fiber. Compared to the stylus trap combined with a high numerical aperture parabolic mirror (*62*), our design offers simplicity and robustness of construction and operation. The design of the parabolic mirror trap is shown in Figure 4.2. The mirror has a focal length of 2 mm, opening of 10.2 mm, and depth of 3.2 mm. It has four rectangular slots for laser access. There is a 1.5 mm central through-hole for the needle electrode. The mirror was machined by single point diamond turning technique by Nu-Tek Precision Optical Corporation, while other parts (including the needle) were machined by the University of Washington Physics Instrument Shop. The needle is attached to a UHV linear actuator to allow axial alignment while in vacuum. Its tip sharpness, which is 6° in our design, determines the depth of pseudo potential and the trapping position of the ion (*61*). The mirror is connected to a high voltage RF potential which, together with the grounded top cross plate and the needle, form the ion trap potential. There are four symmetric

stainless steel plates just above the mirror, which are connected to DC bias voltages to allow radial adjustment of ion position. Taking into account the four slots and the hole in the vertex, this mirror covers a solid angle of 2π steradians. The assembled trap is shown in Figure 4.3.

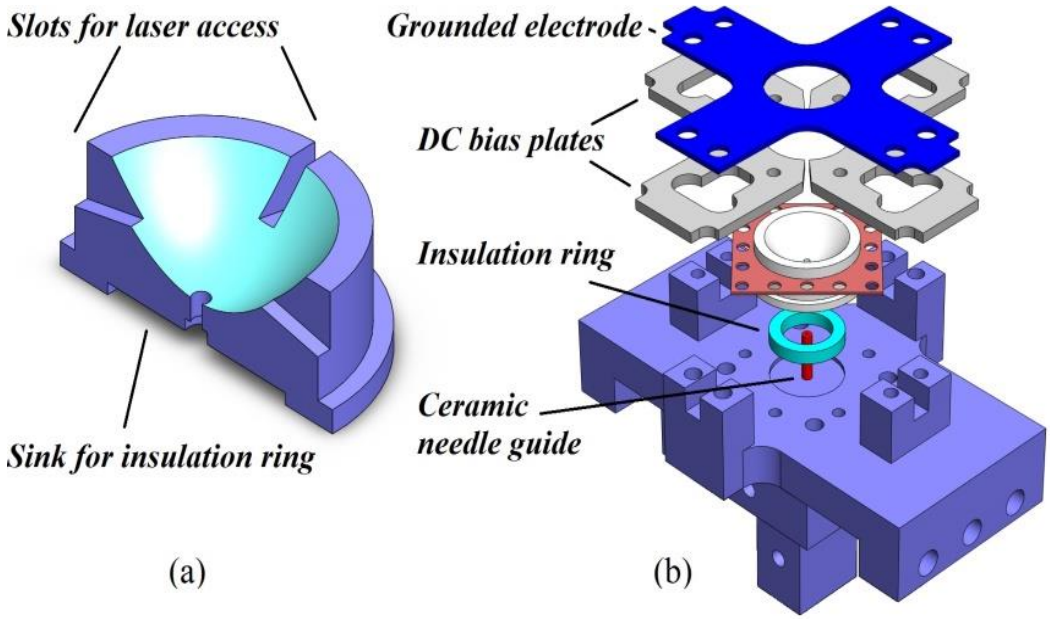

Figure 4.2. Mirror (a) and trap assembly (b) design in SolidWorks. The mirror was machined by the single point diamond turning technique, while other parts (including the needle) were machined by UW Physics Instrument Shop. The parabolic mirror covers a solid angle of 2π steradians when the ion is trapped at its focus.

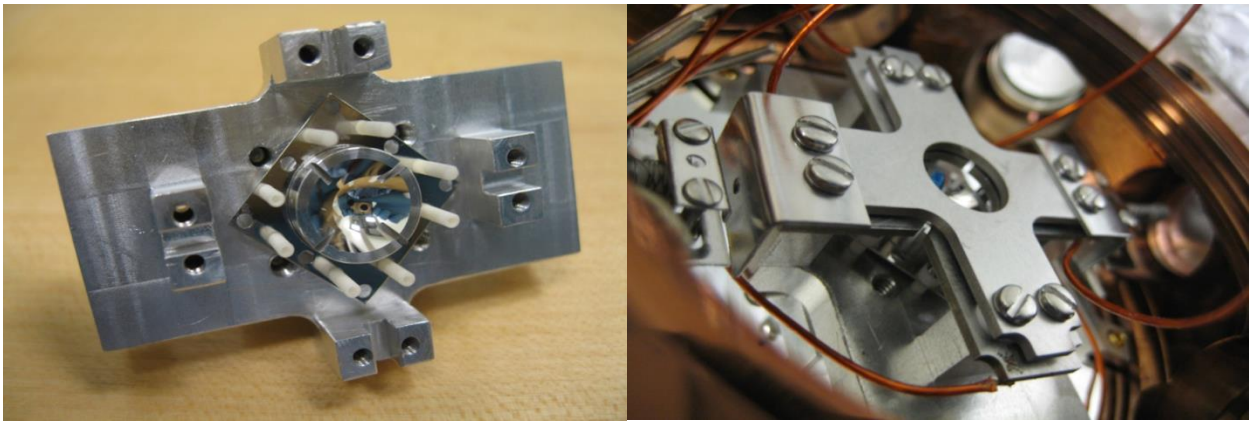

(a) **(b)**

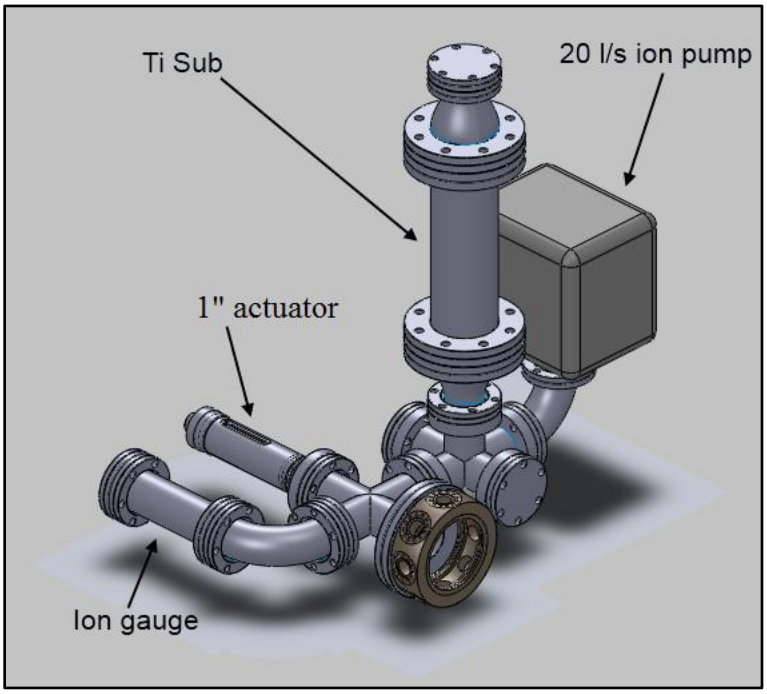

(c)

Figure 4.3. (a) Assembled parabolic mirror trap placed within a vacuum chamber prior to installing the main viewport. (b) The mirror is in the center, partially obscured in the photo by the ground plate. There are two barium ovens with collimation pin holes in horizontal direction. (c) Complete UHV chamber system diagram. There are ion pump, titanium sublimation pump, trapping chamber view port, and ion gauge.

4.2 EQUIPMENT SETUP

We use a 4-1/2” spherical octagon chamber from Kimball Physics to house the trap. Two barium ovens made of ceramic tube are placed horizontally and face toward the trapping center. Two horizontal through holes in the octagon are used for electrical feedthroughs which provide RF trapping potential, four DC bias voltages, and oven heating current. The other six through holes are dedicated to the viewports for lasers access. The simplified diagram of this setup is show in Figure 4.4. Each laser is shuttered by an acousto-optic modulator (AOM) with tens of nanoseconds accuracy.

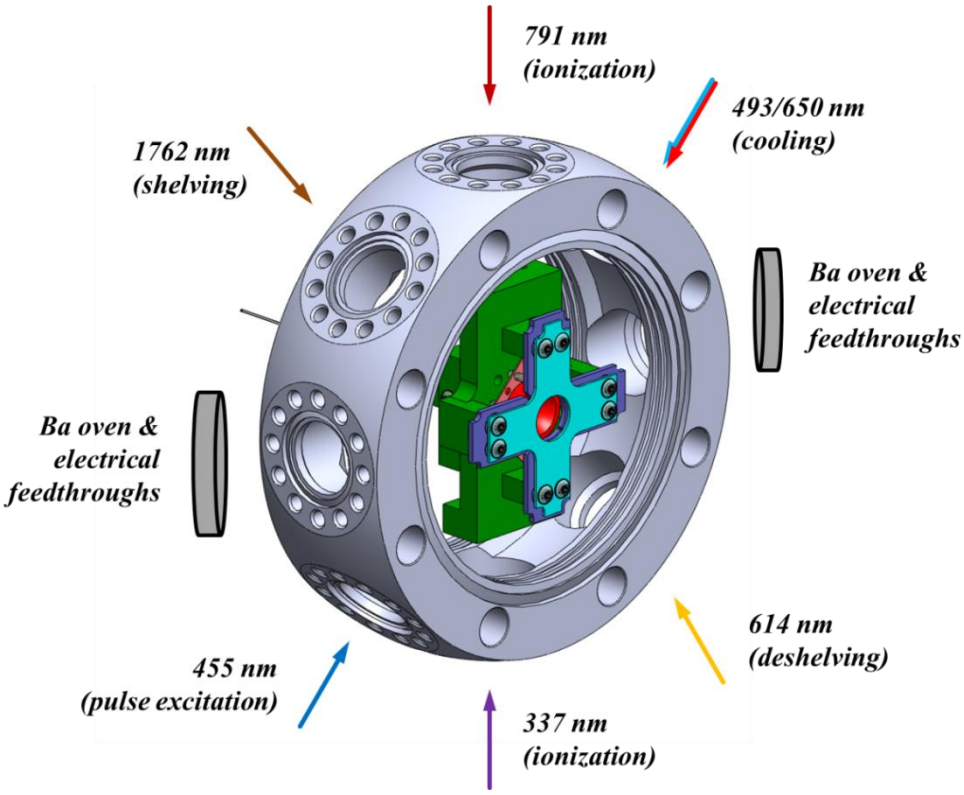

Figure 4.4. The 4-1/2" octagon chamber with 7 different laser access. The 791/337 nm lasers are for ionization, oriented perpendicular to the atomic barium beam directions. The 493/650 nm cooling lasers are delivered in the same optical fiber. The 1762/614 nm lasers are for shelving/deshelving purposes. The 455 nm laser is the mode-locked pulsed laser used for entangled state generation.

We performed a pseudo potential analysis of the parabolic trap using finite element method analysis, and the result is shown in Figure 4.5. The origin of the coordinate system is located at the vertex of the parabola. Confinement in the axial direction is tighter than that in the radial direction, and the trapping depth is approximately 0.06 eV for the RF amplitude of 600 V at 12 MHz. Figure 4.6 is the simulation of distance between ion and needle tip of various needle tip positions along the axis. The ions are trapped about 0.7 mm above the needle tip, and this distance has little dependence on the RF power and the needle's position along the axis. The

trapping potential in the center is almost independent of the optical surface shape, which makes this design universal for different reflector profiles (*61*). The parabolic mirror has a focus at 2 mm, so when the needle tip is placed ~1.3 mm above the vertex of parabola, the ion will be trapped at the focal point.

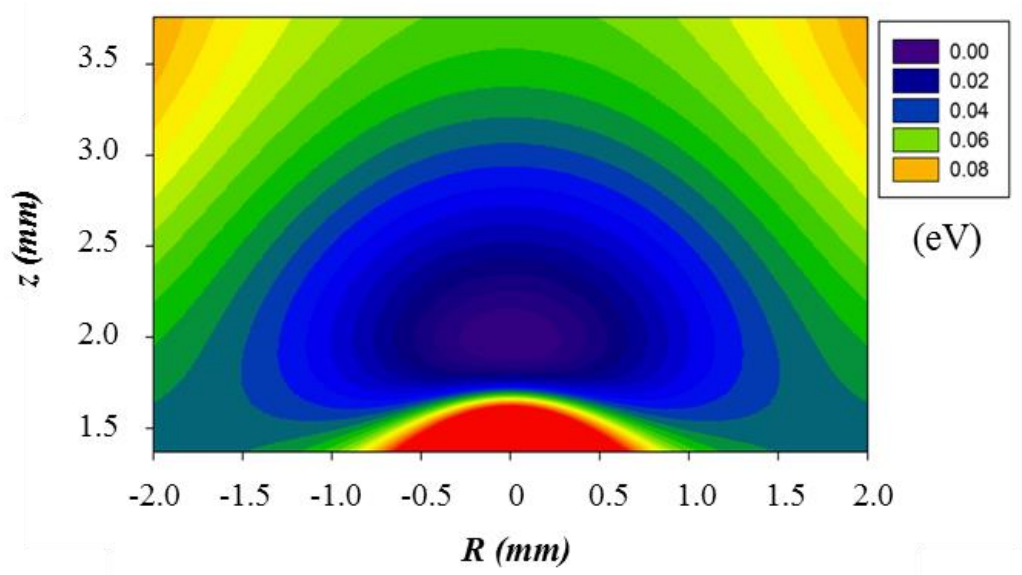

Figure 4.5. Pseudo potential trapping depth simulation. The origin is located at the vertex of the parabola, with *z* axis being the axial coordinate and *r* as the radial. The radial confinement is weaker due to the relatively wide opening of the parabola.

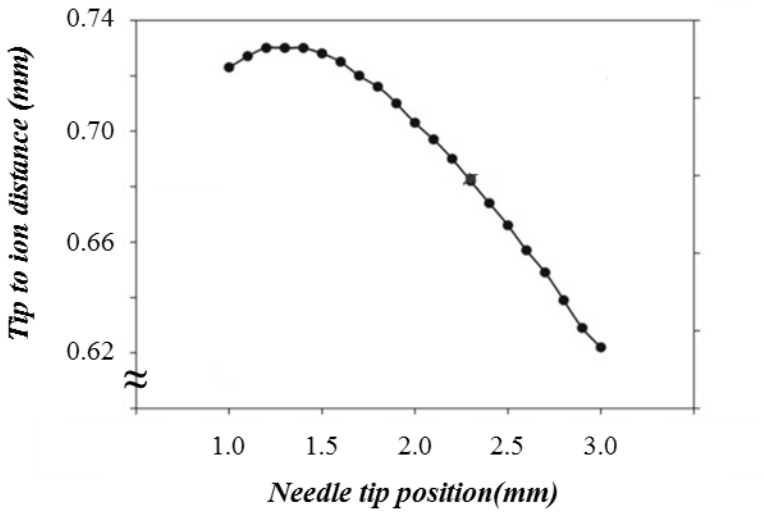

Figure 4.6. The simulation of the distance between the needle tip and the trapped ion at various needle positions. Needle tip position is measured from the vertex of the parabola. Note that the ion to needle tip distance remains relatively constant.

4.3 PERFORMANCE

When we load barium by heating the ceramic tube oven, its evaporation direction is pointing just above the mirror opening, which prevents barium deposition onto the mirror surface. The consequence of this is that the initial trapping position has to be about 2 mm higher than the focus of parabolic mirror. Thus, during the trapping process ions are imaged by a two-stage microscope objective setup instead of the parabolic mirror. After a single ion is trapped, the ion is moved axially using the linear actuator to place it near the focus, then the DC bias voltages are tuned on the four plate electrodes to place ion precisely at the focus of parabola (Figure 4.7). Figure 4.8 shows a series of ion images as its position approaches to the focus of the parabolic mirror.

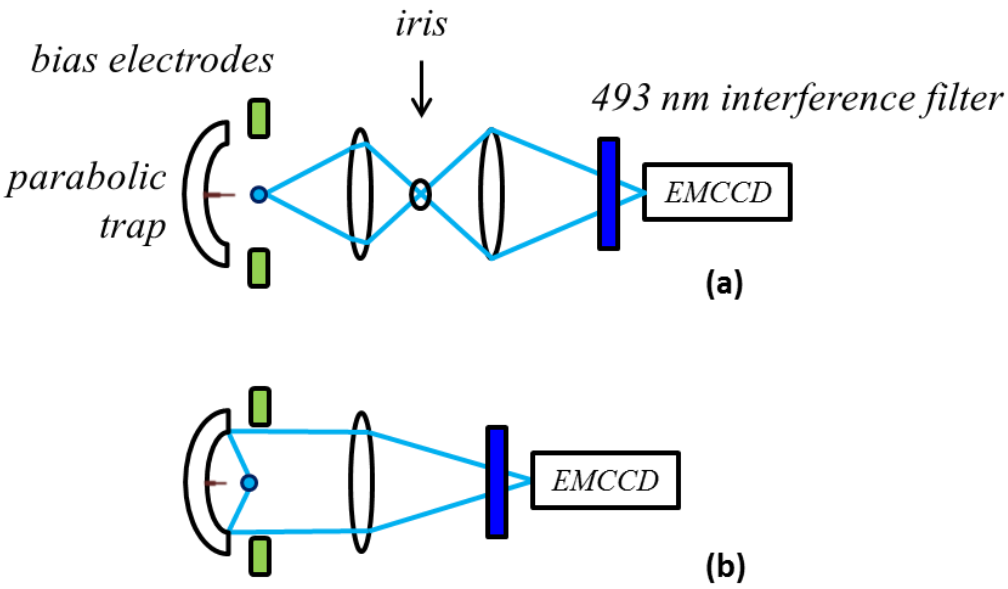

Figure 4.7. (a) A two-stage setup schematic for initial ion trapping. Ion fluorescence is focused by an objective onto the camera. (b) After trapping, the ion is moved to the focus of the parabolic mirror, and then its fluorescence focused by the parabolic mirror followed by a long focal length lens.

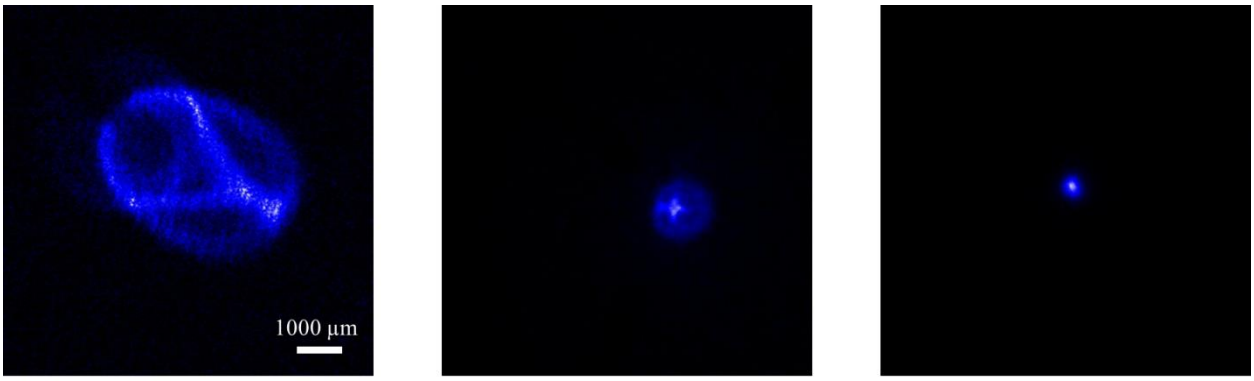

Figure 4.8. A series of single ion images as the ion is moved to the focus of the parabola. The aberration is drastically reduced from (a) as it is moved closer to the focal point of parabola (b and c). The pattern in (a) and (b) comes from the four slots of the parabolic mirror. The magnification of images is 500x.

To measure the photon collection efficiency of the mirror, I used a single photon counting technique which utilities three energy states of barium ion (*61*). Figure 4.9 shows the time sequence of this process. The $6P_{1/2}$ excited state has a lifetime of about 8 ns, while the $5D_{3/2}$ long-live state has a lifetime of about 82 seconds, and the $6S_{1/2}$ is the ground state. By switching between the 493 nm and 650 nm laser excitations, I can generate a single 493 nm photon on demand with essentially 100% reliability. The single photons at 650 nm are strongly attenuated by the 495 nm line filter and result in a negligible background signal.

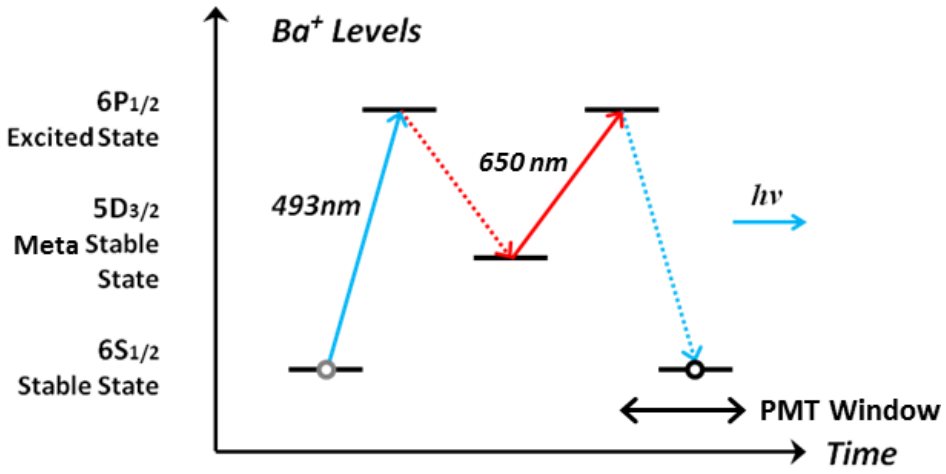

Figure 4.9. Single photon generation pattern. The solid lines represent laser excitation and the dash lines represent spontaneous emissions. The 493 nm laser is turned on for 500 ns to optically pumping the ion into the $5D_{3/2}$ state with essentially 100% efficiency. The 493 nm laser is then switched off, and the 650 nm laser is switched on for 1000 ns which generates one and only one 493 nm photon, which is detected by a PMT. The PMT detection is gated to further reduce the background.

This pattern can be repeated 1 million times in less than a minute, and we measured 47,675 single photon events per 1 million cycles, i.e. approximately 5% overall detection

efficiency of single photon events. This is uncorrected for the PMT quantum efficiency, and the loss in reflection and transmission. To account for these and other factors in order to determine the photon collection efficiency of the mirror, I measured the dependence of the single photon count rate on the solid angle of collection. I placed a calibrated iris in front of an objective lens (10x Mitutoyo Plan Apo Infinity Corrected) to control the aperture size, and directly (i.e. without using the mirror) focused the ion fluorescence onto a PMT. I used the slope of this calibration curve shown in Figure 4.10 to interpolate the photon collection efficiency of our mirror to be about 39% of the total 4π solid angle surrounding the ion. This is a significant improvement over our reflective spherical trap which collects 25% (*61*) and custom-made commercial large NA objective of 10% efficiency (*63*).

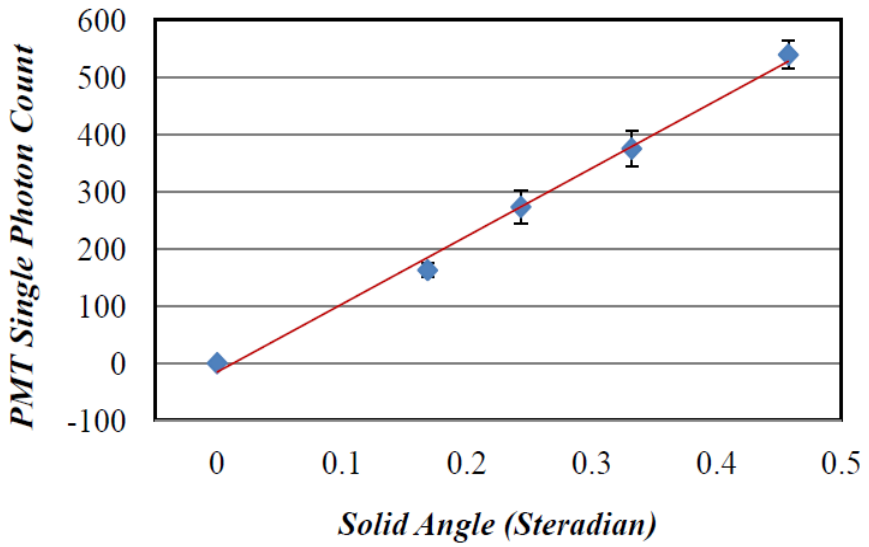

Figure 4.10. PMT counts in 1 million cycles for various solid angles set by the calibrated, adjustable aperture. Red line is the linear fit to the data. Error bars are statistical (standard deviation).

The main hoped-for improvement, when compared to our previous spherical mirror design, is the image quality. To examine the imaging quality of our parabolic mirror, I used a spherical lens of 100 cm focal length to focus the collimated fluorescence from a single trapped ion placed in the focus of the mirror (Figure 4.7b). The ion image spot size I measured is 1065 μm (defined as $1/e^2$ of peak intensity). Dividing it by the system total magnification of 500, I got 2.1 μm as our optical resolution of a single ion. Comparing to the diffraction-limited Airy disc diameter ($1.22 \times \lambda/NA$), which is ~0.61 μm for our geometry at 493 nm, I determined that the mirror performance is about 3.4 times worse than the diffraction limit. This was a somewhat disappointing result at first, and I decided to try to understand the reasons.

4.4 Deformable Mirror Correction

The ion image spot size is vulnerable to ion defocusing and micro-motion, as well as imperfection of parabolic mirror shape. First, I performed ray tracing simulation of point spread function size as a function of defocusing of ion position. The result is shown in Figure 4.11. The accuracy of ion positioning in our experiment is better than 2 μm with the actuator and the bias voltages control. Thus, defocus cannot explain the observed large ion image size.

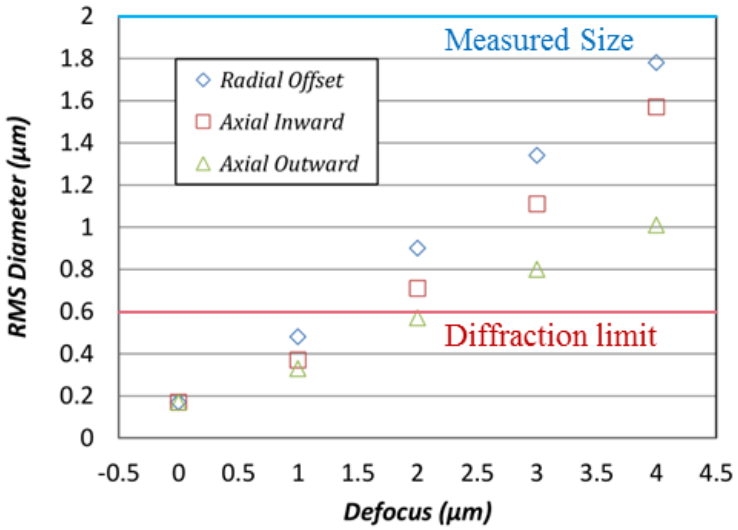

Figure 4.11. Point spread function diameters calculated by ray tracing simulation without diffraction. The spot size stays within diffraction limit (~0.61 µm) when the ion is out of focus by up to 2 µm axially and 1.5 µm radially.

Our next suspect is the imperfection of the parabolic mirror shape. The parabolic mirror is hard to manufacture to precise optical specifications, and measuring its accuracy is not easy as well. Therefore, I adapted a deformable mirror and try to correct the manufacturing imperfection. The deformable mirror I used is a Thorlabs model DMP40. It has 40 independent segments within 11.5 mm pupil diameter, which are arranged as 3 concentric rings and is ideal for my purpose.

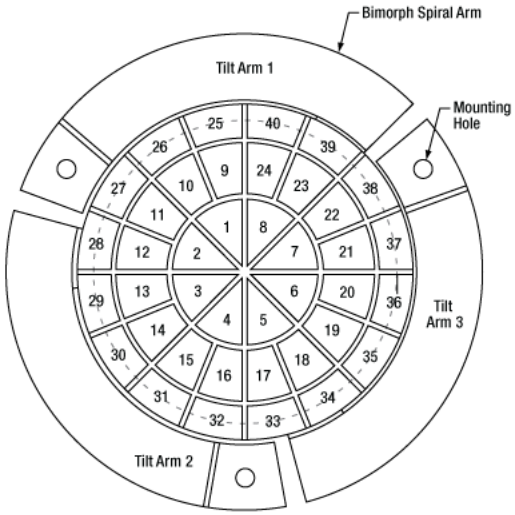

Figure 4.12. Thorlabs DMP40 deformable mirror diagram. Each segment is a piezoelectric disk under a bendable reflective surface, which is controlled by individual voltages to correct wave front aberrations.

The imaging optimization is to minimize the ion spot size in real time. With the deformable mirror placed between the parabolic mirror and EMCCD camera, I focused the ion image 400 mm away from the deformable mirror, such that the total system magnification is 200x. The Thorlabs deformable mirror uses Zernike polynomials to compensate one kind of aberration at a time. The Zernike polynomials are orthogonal polynomials in a unit circle, which simplify the correction process without recursively altering individual segment. Figure 4.13 shows the aberrations that correspond to the first 5 Zernike polynomials (*64*), while Table 3 tabulates these polynomials.

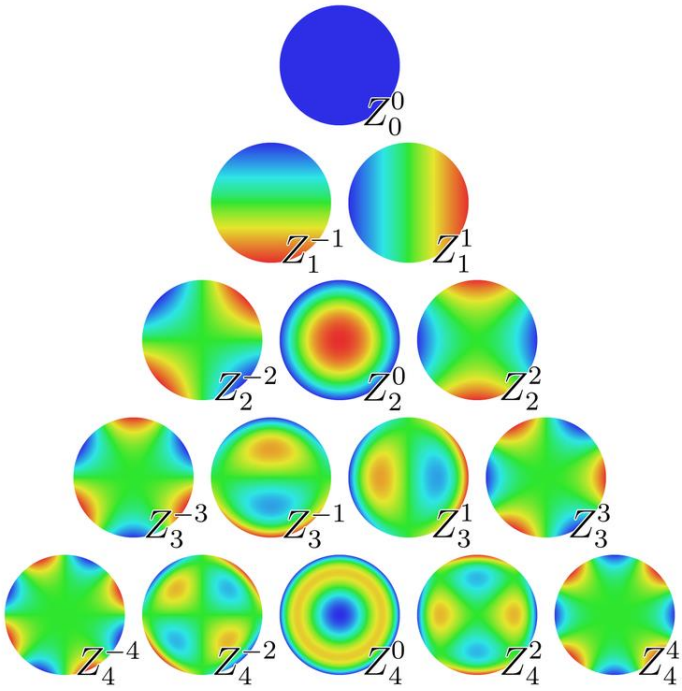

Figure 4.13. The aberration patterns that correspond to first five Zernike polynomials. These functions are widely used in adaptive optics.

Table 3. The list of first five Zernike Polynomials expressions.

		1		
	$2r\sin\theta$		$2r\cos\theta$	
$\sqrt{6}r^2\sin 2\theta$		$\sqrt{3}(2r^2-1)$		$\sqrt{6}r^2\cos 2\theta$
$\sqrt{8}r^3\sin 3\theta$	$\sqrt{8}(3r^3-2r)\sin\theta$		$\sqrt{8}(3r^3-2r)\cos\theta$	$\sqrt{8}r^3\cos 3\theta$
$\sqrt{10}r^4\sin 4\theta$	$\sqrt{10}(4r^4-3r^2)\sin 2\theta$	$\sqrt{5}(6r^4-6r^2+1)$	$\sqrt{10}(4r^4-3r^2)\cos 2\theta$	$\sqrt{10}r^4\cos 4\theta$

The ion image size reduced to about 1.7 μm after optimizing 12 Zernike polynomials parameters for smallest ion spot size. Comparing to the diffraction-limited diameter of 0.61 μm, the overall performance is still about 2.8 times over the diffraction limit. I thus conclude that the

image size is not mostly limited by the mirror geometry. The single ion images with and without the deformable mirror (scaled to the same magnification) are shown in Figure 4.14. In Figure 4.15 I fitted both ion spot images with the Gaussian function. The scale is chosen to make areas under two curves the same, which corresponds to the same photon collection efficiency. The blue curve is a fit to ion image without the deformable mirror, and the red curve is with the deformable mirror correction. The red curve is clearly sharper with smaller width.

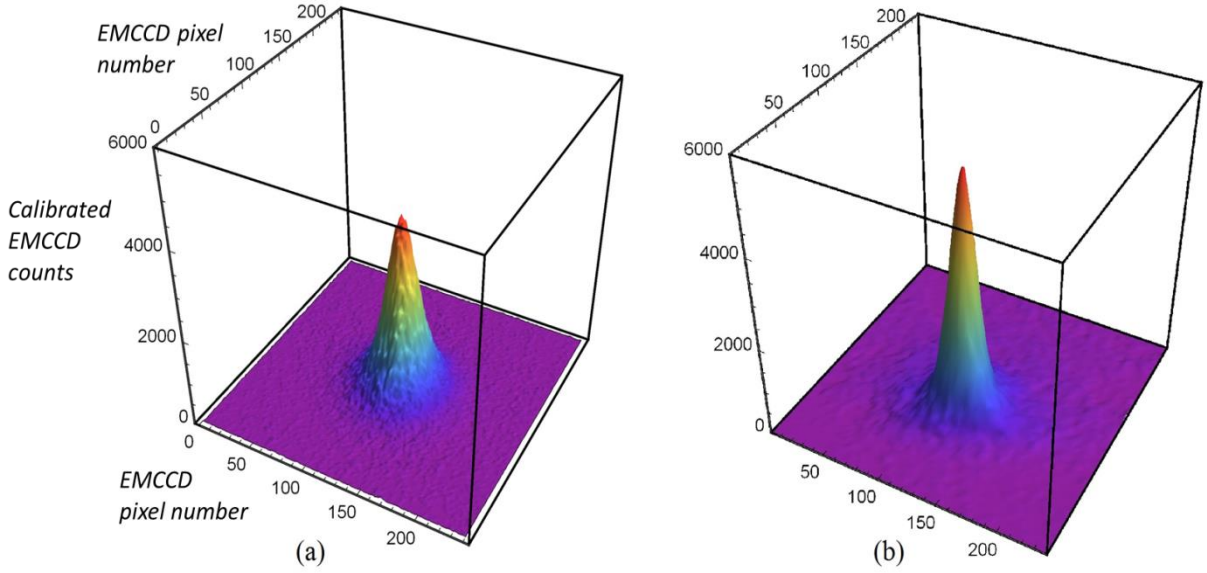

Figure 4.14. Ion intensity distributions. (a) is the original image and (b) is the corrected image after deformable mirror optimization. These images are scaled to account for different magnifications, and the ion spot size is improved from 3.4 to 2.8 times over diffraction limit.

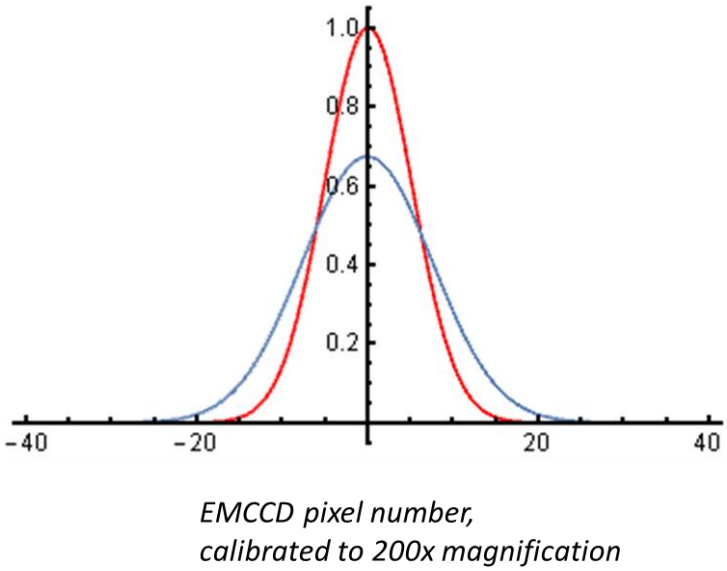

Figure 4.15. Gaussian function fits of two ion intensity distributions. The blue curve is before-deformable-mirror fit and the red curve is after-deformable-mirror fit. The Gaussian width of blue curve is about 1.35 bigger than the width of red curve.

Our ion image spot size is still far from the diffraction limit, and it turns out that it can be explained by analyzing the ion micro-motion in our trap. The ion's motion in one dimension can be approximated as:

$$x(t) \approx [x_0 + x_1 \cos(\omega t)][1 + \tfrac{q}{2}\cos(\Omega t)], \qquad (4.23)$$

where x_0 is the ion's static displacement from the trap center due to the external electric field, x_1 is the ion oscillation amplitude in pseudo potential well, ω is the secular frequency ($\omega = 2\pi \times$ 0.3 MHz in our trap in radial direction), q is the dimensionless coefficient related to RF field and trap dimension ($q = 0.1$ in our case), and Ω is the RF driving frequency ($\Omega = 2\pi \times 12$ MHz) (*57*). There are two components in Eq. 4.24, the slow secular motion with the frequency ω of the pseudo potential well, and the fast driven motion with frequency Ω of the applied RF field, called the micro-motion. When I placed the ion in the focus of the parabola radially through

varying DC voltages, it is displaced from the center of the RF pseudo potential, leading to excess micro-motion. The displacement is measured to be about 40 μm, which results a micro-motion amplitude of $x_0 \times q/2 = 2$ μm. The secular frequency oscillation amplitude for a Doppler cooling Barium ion ($m = 137.9$ amu) is $x_1 = \sqrt{\hbar\gamma/m\omega^2} \cong 0.3$ μm, where $\gamma \cong 2\pi \times 10$ MHz is the natural linewidth of the $6P_{1/2}$ level. The ion trajectory simulation graph is shown in Figure 4.16.

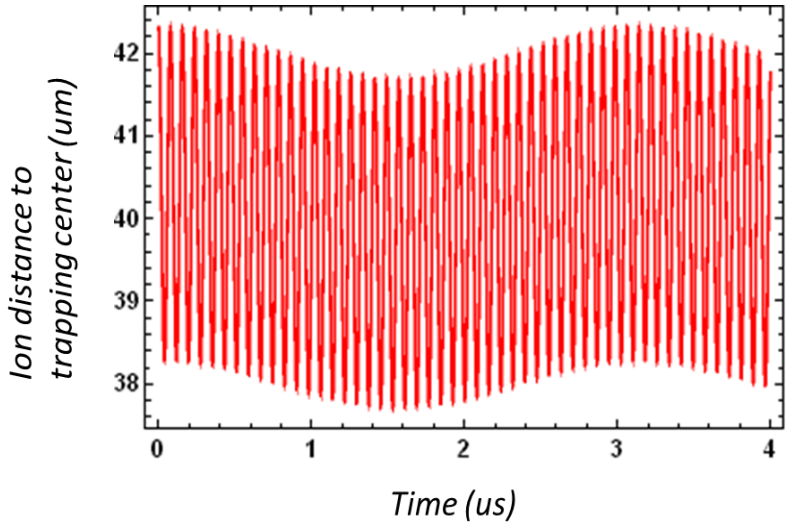

Figure 4.16. The simulation curve of 1D micro-motion when the ion is out of pseudo potential center by 40 μm. Its amplitude is about ten times that of the secular oscillation amplitude.

In our setup, x_1 is smaller than diffraction limit (0.61 μm), but x_0 is quite large, and thus limits the optical resolution. Because micro-motion is due to the non-zero RF driving electric fields when ion is out of trapping center, its amplitude cannot be reduced by Doppler cooling as the secular motion amplitude. This expected x_0 is consistent with the 1.7 μm spot size I have

measured, which means that the observed ion image spot size is predominantly due to the micro-motion oscillation. It should be pointed out that the micro-motion in our case is not one dimensional. Our DC bias electrodes are four plates which individually cover nearly 1/4 of arc around the mirror opening. This setup creates asymmetrical equipotential lines when we apply DC voltages to more than one electrode. The resulting trajectory of ion micro-motion depends on the DC electric potential geometric profile. In a much simplified case, the ion's trajectory in radial plane can be approximated as a portion of hyperbola curve (*65*). As shown in Figure 4.17, there is a phase shift of ion motion between the *x* and *y* axis due to an asymmetrical local DC potential. Also, since our bias voltage plates are not placed in the same plane of ion radially, the bias voltage also drives ion in the axial direction. In our trap geometry, the axial direction force is about 1/2 of radial direction, and $q_x \cong q_z$, which results 1 μm micro-motion amplitude along *z* direction. We cannot observe the axial movement directly, but it contributes to ion image as defocusing effect I described in Chapter 4.4.

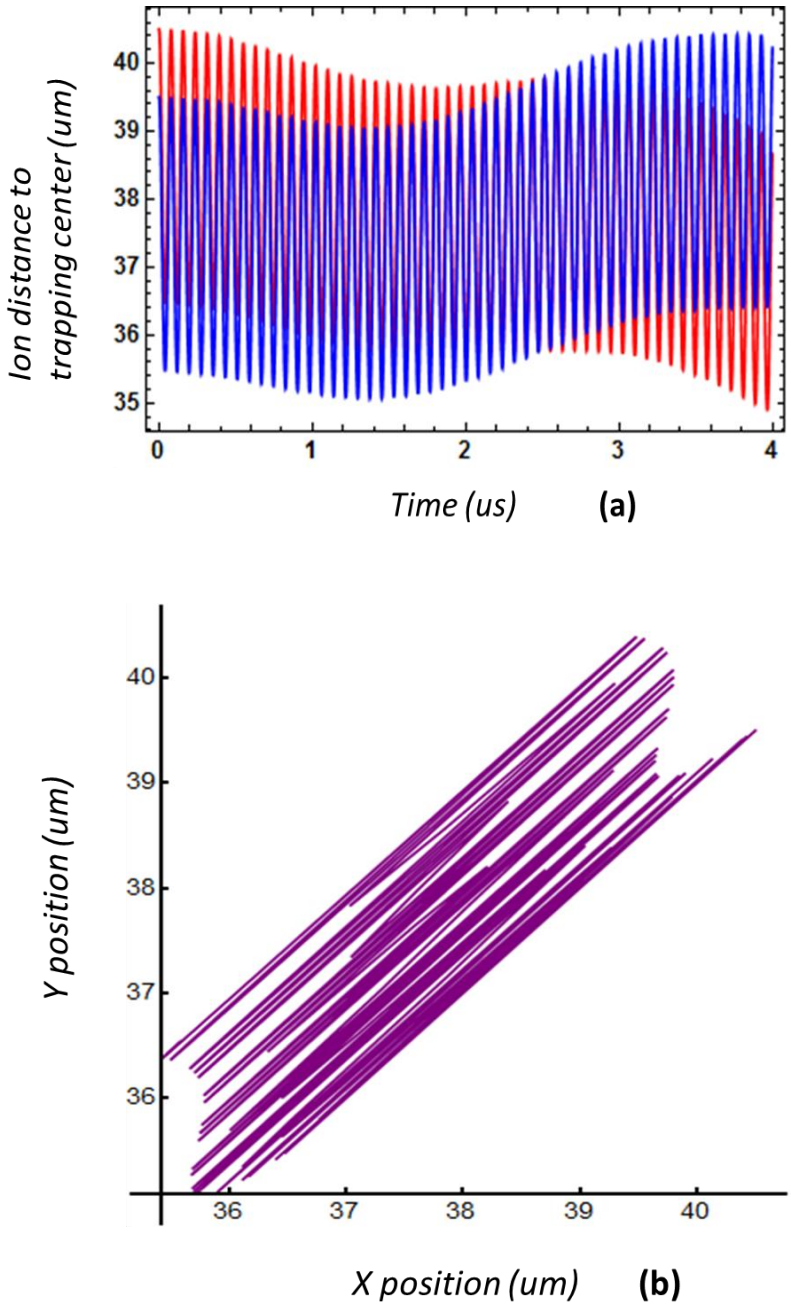

Figure 4.17. 2D simulation of radial micro-motion with some approximations. (a) Blue and red curves are projections on two orthogonal axes. I assume elliptical static equipotential lines from DC bias voltages, which is due to the asymmetry to the pseudo-potential in radial direction. This asymmetric potential changes micro-motion direction by 1°, which corresponds to $\sin 1° \approx 0.02$ amplitude changes. (b) The ion trajectory in the *x*-*y* plane.

This interpretation was further confirmed by performing measurements of the ion image spot size with different NA of the mirror, by placing calibrated, adjustable iris after the parabolic mirror reflection. I observed that the ion image spot size did not change noticeably with reduced NA, meaning that my optical resolution is not limited by diffraction or the mirror shape imperfections.

In summary, I built a reflective parabolic mirror trap covering 50% of solid angle surrounding an ion trapped at the focus of parabola. The measured photon collection efficiency is 39% by single photon counting experiment. I adapted a deformable mirror with 40 independent segments to optimize my ion imaging quality, and found that the spot size of about 2.8 times over diffraction limit is due to the ion's micro-motion. Based on these results, we can improve the next generation of integrated parabolic mirror trap, which includes two in-vacuum piezoelectric actuators to move the needle electrode radially and place the ion in the focus of the parabola. By changing the needle position rather than horizontal bias voltages, we can keep the ion at the center of the RF pseudopotential, thus minimizing the ion micro-motion, so the imaging quality can be improved. The fabrication and testing of this next generation trap is already underway.

Chapter 5. EXPERIMENT II: ION-PHOTON ENTANGLEMENT

5.1 SINGLE PULSE EXCITATION

After characterizing the parabolic mirror trap, I tested its performance of entanglement generation. In this experiment, I use the polarization protocol to generate the ion-photon entanglement because it is easier to implement in barium ion energy levels, and choose the 455 nm pulse laser rather than the 493 nm continuous-wave laser that was used in our previous experiment (*53*). This is because the lifetime of the $6P_{3/2}$ state is about 8 ns, and I need a shorter excitation laser pulse in order to avoid multiple excitations in a single run. In our previous experiment, the excitation rate of our 493 nm laser was only ~20% with a 20 ns exposure time at maximum power, which was unsatisfying (*53*). The multiple excitations lowered the fidelity of entanglement measurement. When the fidelity is below a certain threshold, we cannot observe any quantum phenomena and end up with classical result. To overcome this problem, I adapted the Ti-Sapphire laser, which is a tunable mode-locked pulsed laser. It can output relatively short width pulses of about 2 picoseconds with a repetition rate of 76 MHz. The Ti-Sapphire laser generates the 910 nm pulse train, and a small portion of laser is redirected to a high speed photodiode. The photodiode signals trigger the pulse generator, which outputs synchronized TTL signals. By controlling the trigger delay and width, we can selectively pick a single pulse with the help of the Pockel cell. The setup diagram is shown in Figure 5.1. I used an AOM to increase the extinction ratio to over 10,000:1, and a polarizer to generate π polarized laser pulse.

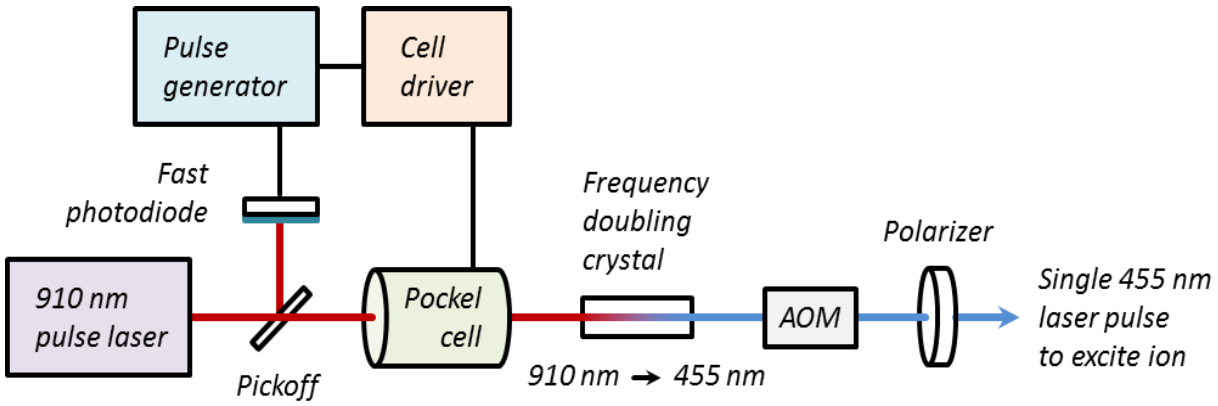

Figure 5.1. The setup for the 455 nm laser single pulse picking. We use a mode-locked Ti-Sapphire laser to generate pulses of about 2 picosecond width with 76 MHz repetition rate. The fast photodiode signals trigger the pulse generator, which generates synchronized TTL signals for Pockel cell driver. The 910 nm laser pulse becomes 455 nm after passing the frequency doubling crystal. An AOM is used to further increase the laser extinction ratio to over 10,000:1, followed by a polarizer which changes the laser to π polarized.

The next task is to measure the excitation rate of a single pulse. In Figure 5.2, there are three possible decay paths for the $6P_{3/2}$ state, which are to the $5D_{5/2}$, $5D_{3/2}$, and $6S_{1/2}$ states, and their respective branching fractions are 21%, 3%, and 76% (*66*). I utilized the fact that the $5D_{5/2}$ state is isolated from the 493 nm and 650 nm laser cooling cycle, making it a "dark state". After shining a single 455 nm pulse at a time, I measured a barium ion's fluorescence by turning on the cooling lasers, and repeated this process one million times to calculate the probability of dark state occurrence. This measurement is faster than single photon counting method if the expected excitation rate is far from 100%. The measured single pulse excitation rate fluctuated between 10% ~ 40%. This large uncertainty is due to the fluctuation of the 455 nm laser pointing, which is about submillimeter scale and visible to the naked eye. The average excitation rate in my measurement is about 20%. This number is the same as when using a 20 ns 493 nm laser

exposure before, but it is guaranteed that now a single excitation is produced, which is crucial for the entanglement experiment.

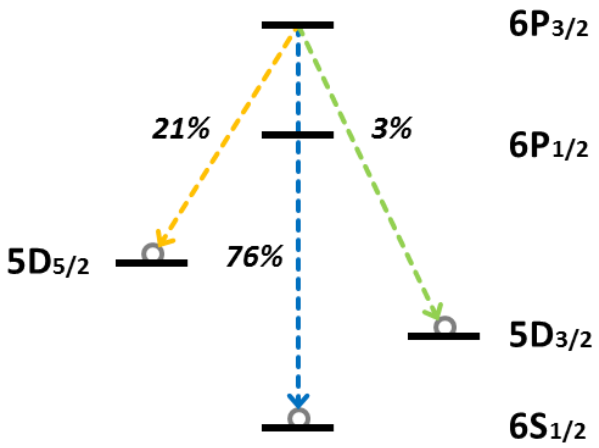

Figure 5.2. Singly ionized barium energy levels. The $6P_{3/2}$ and $6P_{1/2}$ state have lifetime about 6 ns and 8 ns, while the $5D_{5/2}$ and $5D_{3/2}$ states have lifetime around 30 and 80 seconds. When the 493 nm and 650 nm cooling lasers are turned on, the $5D_{5/2}$ state becomes the dark state.

Besides the state excitation, I also need to measure the ion qubit state. The state readout utilities the $5D_{5/2}$ level as a long-live state ($\tau \cong 30$ seconds) as described in Chapter 2.5. When the ion ends up in the $5D_{5/2}$ state, the fluorescence from the ion cooling cycle disappears. A 1762 nm fiber laser can drive transition from $6S_{1/2}$ to this state. The fiber laser has a narrow linewidth of serval hundred hertz, which allows selective excitation for one of two splitting ground states. If we vary the exposure time of the 1762 nm fiber laser to the barium ion, we will drive Rabi oscillation between $6S_{1/2}$ and $5D_{5/2}$ states. To find the resonant 1762 nm laser frequency and the π pulse width, I first optically pumped the ion to a single qubit state by changing the cooling 493 nm laser to σ^+ polarization. The resonant 1762 nm laser frequency is found by scanning its frequency to search for highest ion shelving probability. After the resonant frequency is found, I

incrementally increased the 1762 nm laser exposure time, followed by the ion state readout. The Figure 5.3 shows the experimental result of ion state measurement with various 1762 nm laser exposure times. The *y* axis is the probability of finding the ion in the "dark state" during the normal cooling cycle. The Rabi frequency Ω is about $2\pi \times 120$ kHz and a π time is about 8 µs. Thus, by turning on the 1762 nm laser for 8 µs, followed by the Doppler cooling lasers, I can measure (readout) the ion qubit state from the fluorescence detection. The resulting curve is the shelving probability fitted to sinusoidal Rabi oscillation curve with small decay due to the ion temperature and laser noise, and it is of 95% π pulse shelving efficiency.

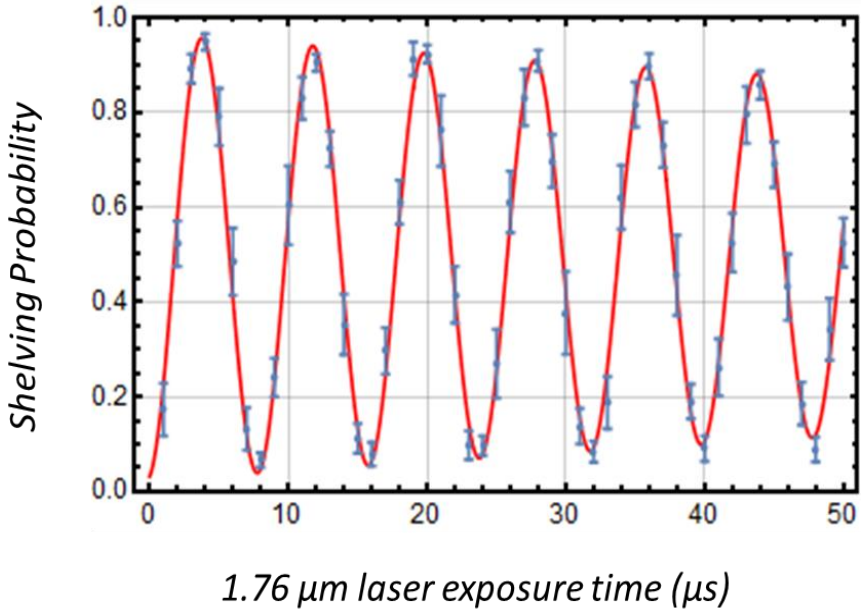

Figure 5.3. The probability that the ion is "dark" for different widths of 1762 nm laser pulse, which drives the Rabi oscillation between $6S_{1/2}$ and $5D_{5/2}$ states. The ion flops back and forth as pulse duration increases. The maximum excitation probability is about 95%, which is limited by optical pumping efficiency, laser noise, and state decoherence with time.

5.2 POLARIZATION QUBIT

In Chapter 3.1, I showed that the maximum CHSH inequality violation occurs when the spin of electron 1 is measured at $(0, \pi/2)$ basis and the spin of electron 2 is measured at $(\pi/4\,, 3\pi/4)$ basis. To find its corresponding ion-photon counterpart, let us review the barium ion energy levels and their photon emission polarizations:

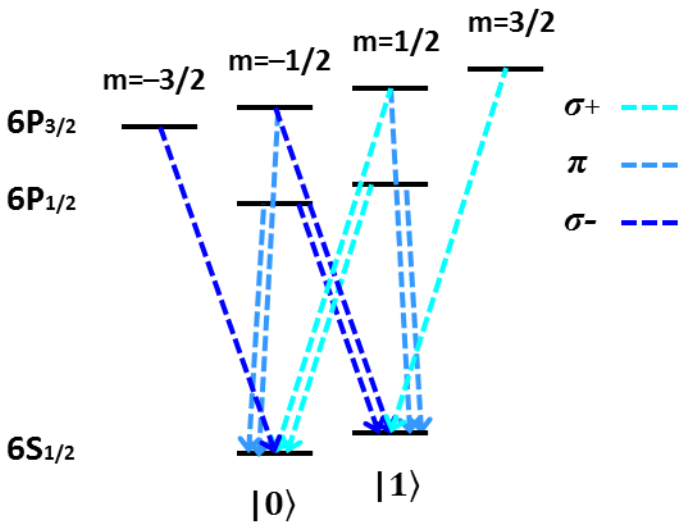

Figure 5.4. Different photon polarizations of various dipole transitions in barium ion. When $\Delta m = \pm 1$, photon is emitted with angular momentum ±1 to the quantization axis, which is circular $\sigma^{\pm}$ transition. When $\Delta m = 0$, photon is emitted as linearly polarized π transition.

Only the energy levels relevant to our entanglement experiment are shown in Figure 5.4. There are three possible photon polarizations for the dipole transitions, and their respective radiation distribution patterns are shown in Figure 5.5.

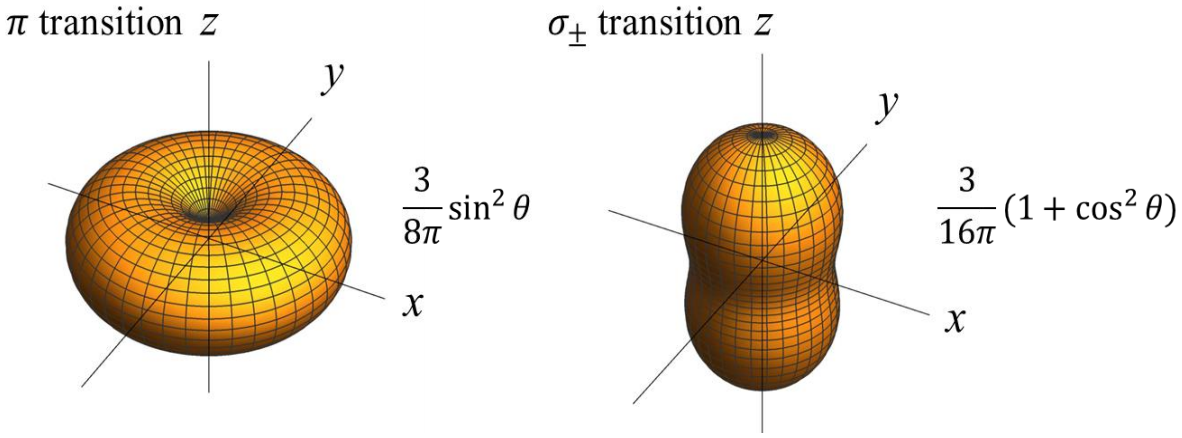

Figure 5.5. Radiation distribution patterns of dipole transitions. For π transition, it is equivalent to the dipole radiation of the electron moving along the *z* axis. For $\sigma^{\pm}$ transition, it is equivalent to the dipole radiation of the electron circulating in the *x*-*y* plane. The quantization axis is along the *z* axis.

Because the solid angle covered by my parabolic mirror is 39%, the method used in our previous paper cannot be applied, which utilizes the fact that π and $\sigma^{\pm}$ transitions are orthogonally linearly polarized on the *x*-*y* horizontal plane when viewed at 90° to the quantization axis (*53*). Due to mode mismatching, π polarized radiation cannot be coupled into a single mode fiber collinear with the quantization axis (as *z* axis shown in Figure 5.5) (*67*). Therefore, the photon polarizations after fiber coupling are $\sigma^{\pm}$ radiations only, which become linearly polarized and perpendicular to each other after passing a quarter-wave plate (QWP). The entanglement between the ion and photon is generated by shining a π polarized 455 nm laser pulse to drive the ion to two $6P_{3/2}$ states with equal probability. While the ion decays, π polarized photon will be attenuated by single mode fiber coupling, and the ion will be entangled as

$$|\psi\rangle = (|0\rangle_{ion}|\sigma_+\rangle_{pho} - |1\rangle_{ion}|\sigma_-\rangle_{pho})/\sqrt{2}, \quad (5.24)$$

after single mode fiber coupling. The polarization of $\sigma^{\pm}$ radiation is not uniformly distributed as circularly polarized in space. As azimuthal angle increases, it is getting more and more elliptical and becomes linearly polarized on the horizontal plane, as shown in Figure 5.6.

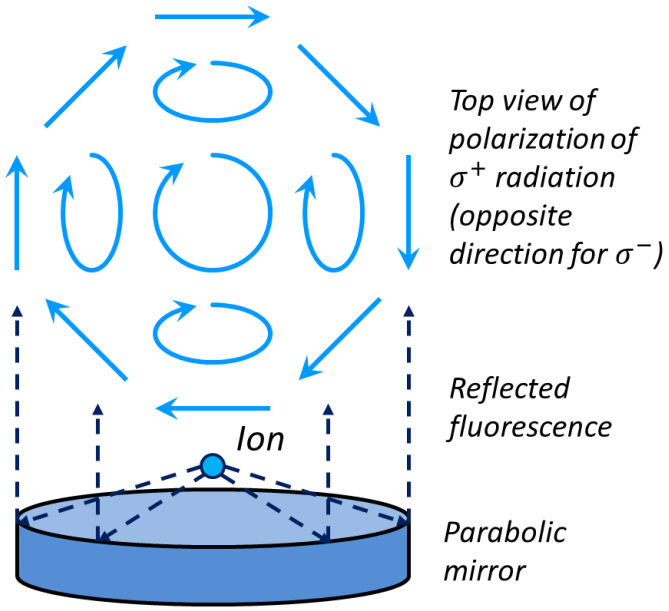

Figure 5.6 The reflected radiation polarization profile of $\sigma^{\pm}$ transitions. It is only perfectly circular along the quantization axis, and becomes more and more elliptical as azimuthal angle increases. The dark blue arrows show photon traveling directions, and light blue arrows show the polarization patterns at different place.

Luckily, a single mode fiber is capable of reshaping the $\sigma^{\pm}$ radiation pattern into a right-handed/left-handed circularly polarized photon. When the fiber is aligned to the radiation's quantitation axis, the elliptical fields in the opposite directions will destructively interfere, like in the π radiation case during mode-matching process, which results in pure circularly polarized light out of the optical fiber (*67*). In order to measure the photon polarization state evolution through fiber coupling, I need to investigate the birefringence effect of the single mode optical

fiber. With Jones matrix model, we can represent photon's polarization state as a 1x2 complex vector, and polarization-changing facilities, i.e. wave plates, as 2x2 complex matrices (*68*). Table 4 shows some example matrices of basic polarization-changing components, which are similar to 1/2 spin matrices in quantum mechanics.

Table 4. Jones matrices used in some basic linear polarization transformations.

Photon polarized in 0° *(x)* / 90° *(y)* / 45°	$\begin{bmatrix}1\\0\end{bmatrix}$	$\begin{bmatrix}0\\1\end{bmatrix}$	$\begin{bmatrix}1\\1\end{bmatrix}/\sqrt{2}$
Linear polarizer at 0° / 90° / 45°	$\begin{bmatrix}1 & 0\\0 & 0\end{bmatrix}$	$\begin{bmatrix}0 & 0\\0 & 1\end{bmatrix}$	$\begin{bmatrix}1 & 1\\1 & 1\end{bmatrix}/2$
QWP with fast axis at 0° / 90° / 45°	$\begin{bmatrix}1 & 0\\0 & i\end{bmatrix}$	$\begin{bmatrix}1 & 0\\0 & -i\end{bmatrix}$	$\begin{bmatrix}1 & i\\i & 1\end{bmatrix}/\sqrt{2}$
HWP with fast axis at 0° / 90° / 45°	$\begin{bmatrix}1 & 0\\0 & -1\end{bmatrix}$	$\begin{bmatrix}1 & 0\\0 & -1\end{bmatrix}$	$\begin{bmatrix}0 & 1\\1 & 0\end{bmatrix}$

Assuming I have a σ^+ photon, it becomes right-handed circularly polarized after coupling into the single mode fiber, and can be expressed as $[1, i]/\sqrt{2}$ regardless of the axis I choose. After passing through an optical fiber, the birefringence will introduce a phase shift θ along a certain axis, and the photon polarization becomes $[1, ie^{i\theta}]/\sqrt{2}$ along that axis. If I place a QWP with fast axis at 45° to this axis, the photon polarization becomes $[1 - \cos\theta - i\sin\theta\,, -\sin\theta + i + i\cos\theta]/2 = [1,1]/\sqrt{2}$ in Jones calculus notation, which is linearly polarized. When a σ^- photon is transmitted in the same optical fiber, its polarization will become $[1, -1]/\sqrt{2}$, which is also linearly polarized and perpendicular to σ^+ after passing the optical fiber and QWP. If I keep the optical fiber from any physical perturbation, the

birefringence stays constant. I can use a QWP to change $\sigma^{\pm}$ photons into perpendicular linear polarization bases and a polarization beam splitter (PBS) for the orthogonal measurements. I have coupled the right and left handed circularly polarized laser beams into a single mode fiber, and verified this result.

As the photon is measured linearly polarized at angle θ (which is calibrated to spin up state by wave plates such that $\theta = 0$ corresponds to the ion qubit state $|1\rangle$), the ion will collapse into $(\cos\theta\,|1\rangle + e^{-i\delta}\sin\theta\,|0\rangle)$ quantum state. Here, δ is the relative phase due to the energy splitting of states and the time elapsed between photon emission and state readout measurement. Because I did not perform the qubit state rotation, δ is a constant which does not change the result of the ion state readout.

5.3 Entanglement Generation Setup

For the polarization qubit generation and measurement, it is important to align the external magnetic field direction to our parabolic mirror's optical axis. It is not only initializing the ion qubit state more accurately, but also providing the symmetric solid angle coverage for the polarization measurement. In order to align the magnetic field direction at the ion trapping position, I place three wire loops along the *x*, *y*, and *z* axis as shown in Figure 5.7. Each wire loops is connected to a DC power supply, and I can adjust the magnetic fields in all three dimensions by turning their currents. The alignment is done with the help of selection rules of dipole transitions again. In the cooling cycle shown in Figure 2.6, when the 650 nm laser is of σ^{+} or σ^{-} only, the ion will eventually become dark because some transitions is not driven in the cooling cycle. This selective driving laser can only point along the optical axis, because we

cannot distinguish σ^+ and σ^- transitions when the laser is perpendicular to the quantization axis. I use the 650 nm laser rather than the 493 nm to avoid the strong reflection. The top and the side coils both have 10 loops, while the coil along the optical axis has about 150 loops. After shining the σ^+ 650 nm laser along the optical axis, I tuned the currents running in each coils. When the photon count of the PMT is minimized, that means the ion is in the $m = 1/2$ or $m = 2/3$ states of $5D_{3/2}$ level, and the magnetic field is aligned to the σ^+ 650 nm laser along the optical axis. The resulting photon counts ratio between σ^+ and evenly distributed polarized laser is about 100:2.

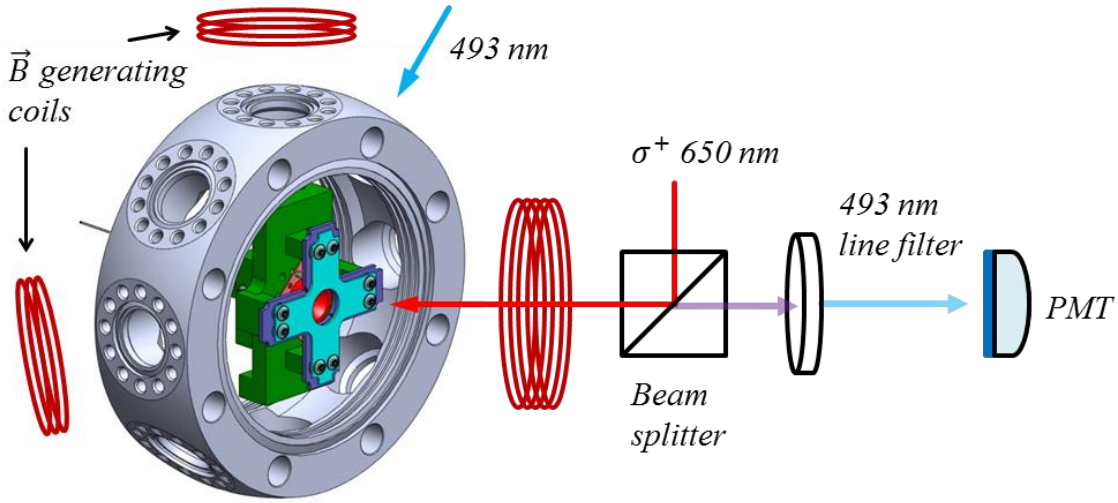

Figure 5.7. External magnetic field alignment setup of three wire loops. The driving σ^+ 650 nm laser is pointing along the symmetric optical axis of parabolic mirror. I tuned the currents of three magnetic field generating coils to minimize the photon counts on the PMT.

After the alignment of quantization axis, we can correctly measure the polarization of photon. The entanglement setup is illustrated in Figure 5.8. The orthogonal bases for photon polarization measurement are realized by placing a QWP and a half-wave plate (HWP) after the

optical fiber. The QWP changes two circularly polarized photons into perpendicularly linearly polarized photons, and the HWP rotates the linearly polarized photons to any angle. To change e measurement basis for photon polarization, the HWP is rotated instead of PBS for easy adjustment. The photon polarization is detected by two PMTs placed at both outputs of the PBS.

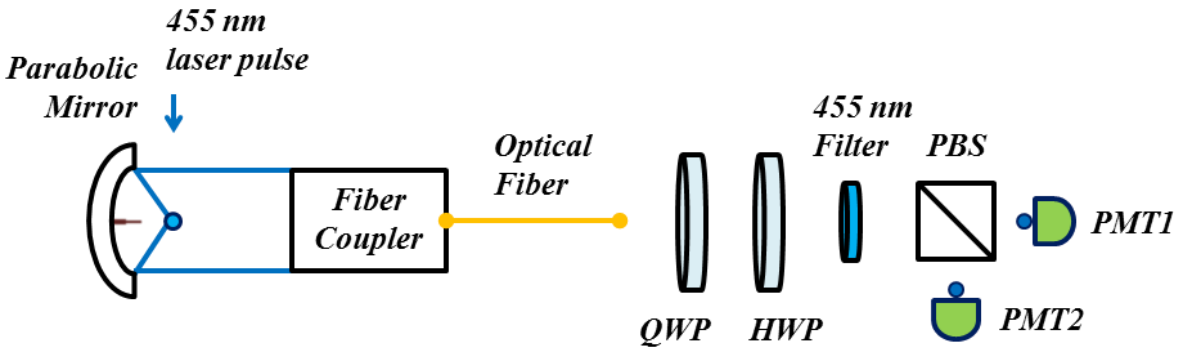

Figure 5.8. Optical setup for ion-photon entanglement measurement. QWP angle is calibrated and fixed. I rotated HWP to different angles in order to change the photon detection basis. A data point is registered only when one of PMT detects a photon.

The 455 nm photon radiated from the trapped ion is collimated and fiber coupled through an off-axis parabolic reflective fiber coupler from Thorlabs, whose clear aperture is 11 mm.

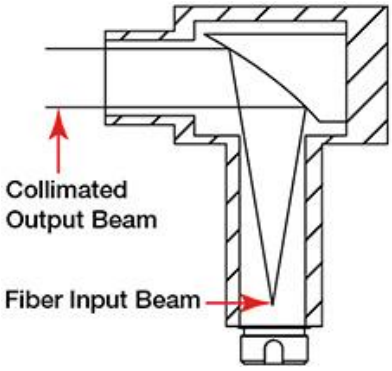

Figure 5.9. Off-axis reflective parabolic fiber coupler. It is not sensitive to wavelength and is designed for coupling a collimated beam.

The complete entanglement generation and measurement process contains following steps, which is illustrated in Figure 5.10:

1. Cooling (10 μs) – including the 493 nm and 650 nm lasers
2. Single photon generation (20 μs) – as described in Chapter 4.3, which generates equal distribution superposition ion qubit state, the initial state for entanglement generation
3. Excitation – 455 nm single pulse excitation with the mode-locked laser, preventing multiple excitations with a 20% excitation rate
4. Spontaneous emission – 3/4 branching ratio for $6P_{3/2} \rightarrow 6S_{1/2}$ transition, which generates a single 455 nm photon in an entangled state with the ion (*66*)
5. Photon detection (100 ns) – photon will be detected by two PMTs after two PBS outputs; proceeds steps 6 and 7 if a photon is detected, otherwise jumps to step 8
6. Ion qubit state readout (50 ms) – a 1762 nm π pulse followed by the 493 nm and 650 nm lasers cooling and fluorescence detection

7. Record – each data point contains three parameters: HWP angle, PMT number that detected a photon, and the ion qubit state readout result.
8. Deshelving – the 614 nm laser drives the ion out of $5D_{5/2}$ state, which the ion could fall into during 455 nm excitation or state readout steps

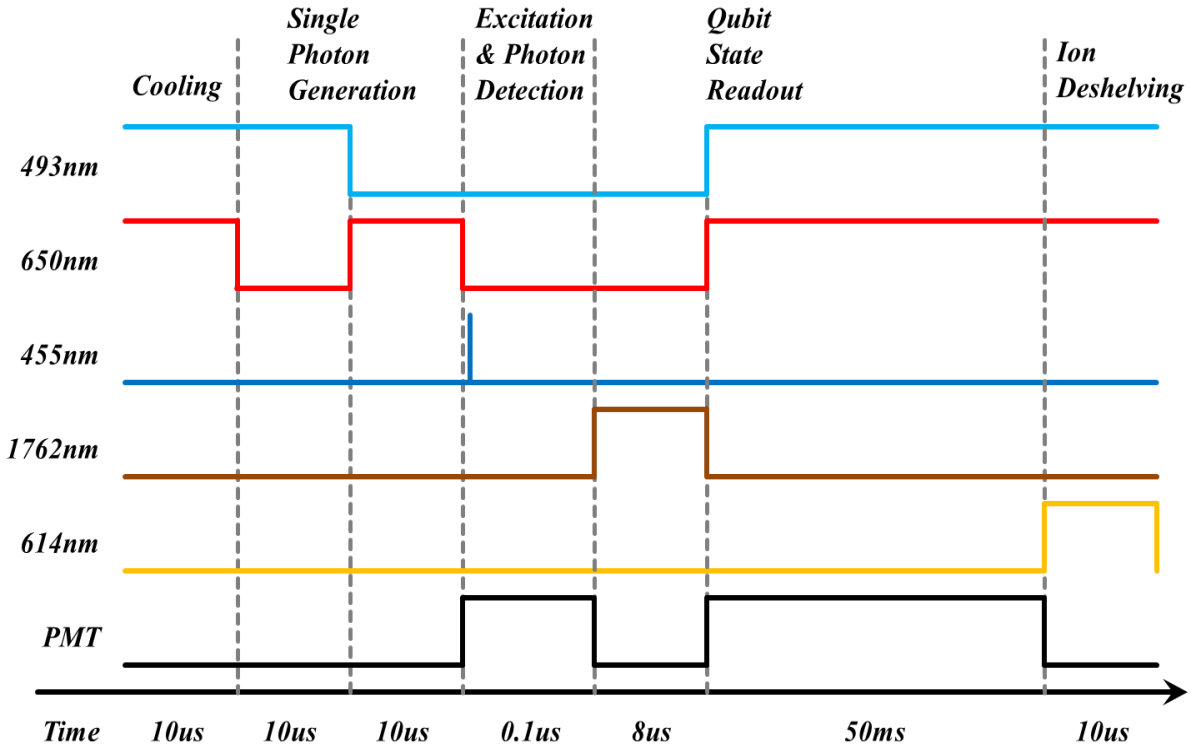

Figure 5.10. Lasers and PMT sequencing diagram of entanglement experiment. It begins with cooling and single photon generation steps to initialize the ion to the evenly distributed qubit states. Then single pulse of the 455 nm mode-locked laser is triggered, and PMT detecting windows is of 0.1 μs. Only when PMT detects a photon, the qubit state readout is executed. The last step is the deshelving the ion from the $5D_{5/2}$ state, which is the long-lived state in 455 nm excitation or state readout cycle.

The whole process is programed in the LabVIEW software, which controls the National Instrument data acquisition card with 10 MHz onboard clock, and the shortest time step in Figure

5.10 is 0.1 μs. The uncertainty of the 455 nm laser pulse arrival time is within 13 ns, which is the separation between two pulses. The entanglement detection rate is about 1 Hz at present in our setup.

5.4 Entanglement Measurement

Combing all the techniques I mentioned above, I performed the entanglement measurement between single ion and single photon. The data I collected includes three pieces of information: HWP angle, PMT number, and ion qubit state readout results. In Figure 5.11, the *x* axis is the photon polarization angle detected by PMT, which is derived from the HWP angle for intuitive understanding, while the *y* axis is the conditional probability of ion qubit state readout.

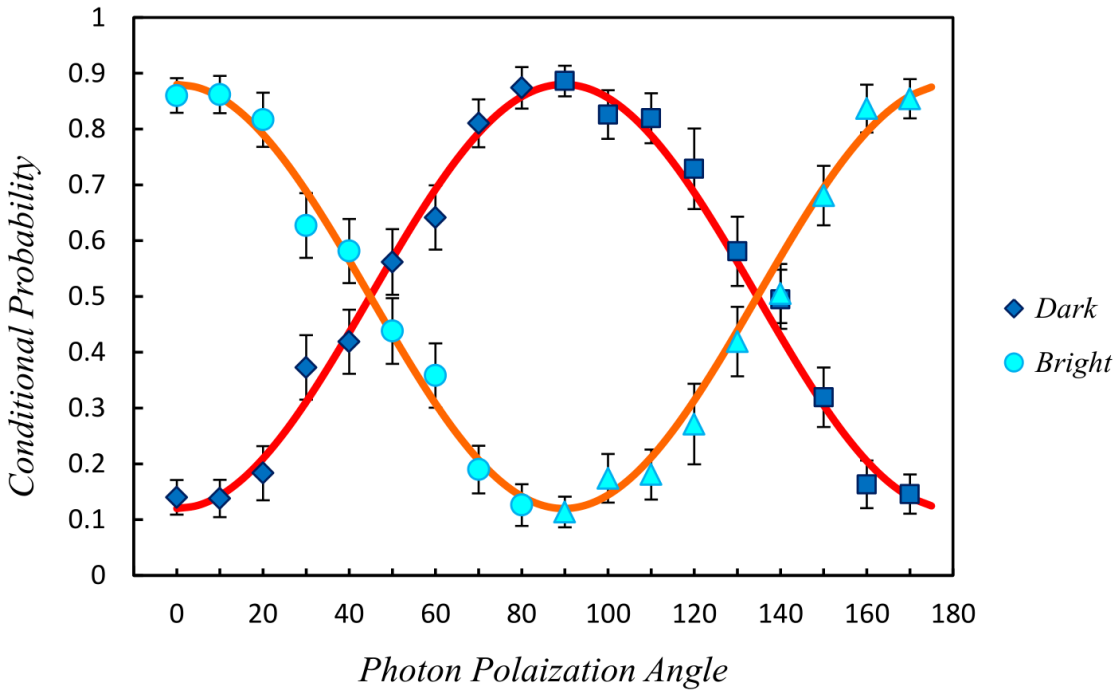

Figure 5.11 Ion-photon entanglement measurement result. When HWP angle is rotated from 0° to 40°, the PMT 1 detection basis is changing from 0° to 80° and the PMT 2 is changing from 90° to 170°, because they are place at different outputs of PBS. The error bars are statistical.

At each HWP angle, a single measurement data consists of 200 photon detection events combing from both PMTs, and statistical error bars are derived from 3 data sets. I then calculated the percentage of bright/dark states when PMT 1 registered a photon, and did the same for PMT 2. This gives me the oscillating conditional probability as the qubit states rotate with the photon polarization detected. The polarization of PMT 1 and PMT 2 measurements are orthogonal, so they are shifted by 90° in Figure 5.11. I changed the measurement basis of photon polarization in 10 degree increments. This calibrates the wave-plates readings and gives me a clear picture of correlation curve. The red and orange curves are fitted with $\sin^2\theta$ and $\cos^2\theta$ of detection probability. I calculated the contrast of my correlation measurement as

$|P_{bright} - P_{dark}|/|P_{bright} + P_{dark}| \cong 0.76(0.03)$, which is above the classical limit of 50% and the 71% threshold of Bell's inequality violation test (*44*). The number is lower than our previous measurement using lens to directly focus the ion fluorescence without optical fiber, which is 84% (*53*). Comparing these two experiment setups, the decrease of fidelity may be due to the optical fiber birefringence changes from environment thermal/mechanical perturbations. Another factor is the polarization inhomogeneity from mirror reflection. Theoretically, the $\sigma^{\pm}$ dipole radiations will result in a circularly polarized light after mode-matching photon into a single mode optical fiber. Realistically, my mirror has four apertures for laser access, and this radial asymmetry leads to inhomogeneity mode-matching condition of $\sigma^{\pm}$ radiation reflection. This results non-ideal right-handed/left-handed circularly polarized photons after fiber coupling, which are not perfectly orthogonal to each other. The other factors causing the fidelity loss include the state readout inaccuracy, wave plate imperfection, and the PMT background counts. The Rabi oscillation of 1762 nm shelving is not ideal, which only reaches 95% accuracy. The polarizer, QWP, HWP, and PBS also contribute 4% polarization imperfection in state initialization and detection. The PMT background noise gives fake signals, which is about 2%.

Chapter 6. OUTLOOK: BELL'S INEQUALITY VIOLATION TEST

6.1 ION-ION ENTANGLEMENT

One of our objectives is to close the locality loophole and the detection loophole in the same experiment, which needs a system capable of generating remote entanglement, and high detection efficiency. The state-of-art high numerical aperture lens setup only collects up to 10% of total 4π solid angle, which generates remote ion-ion entanglement at 4 Hz in one meter distance (*63*). The result from my experiment shows that the photon collection efficiency of trapped ion is improved with the parabolic mirror trap by four folds, and the entanglement between the trapped ion and its photon is verified. With this setup, I can generate entangled state between an ion and a photon through optical fiber coupling, and this distance is limited only by optical fiber length. If we could wire an optical fiber between our laboratory in Physics building and one in the Center for Experimental Nuclear Physics and Astrophysics (CENPA), which is roughly 1 km away, we would have about 3 μs window for qubit state detection to close the locality loophole. The detection loophole can be closed by establishing the ion-ion entanglement through photon interaction (*69*). The idea is to generate two ion-photon entangled pairs at two distant locations, and entangle these two photons through a partial Bell state measurement, for example using a non-polarizing beam splitter. When a certain condition is met (which I will discuss below), these two ions will be entangled in a particular state. The advantage of this protocol is the entanglement is transferred from photons to ions, which have detection efficiency near unity. The drawback is the low entanglement generation rate between two photons, which is

greatly improved in my parabolic mirror trap. There are experiments with similar idea which generate entangled ion-ion state in shorter distance about 1 meter distance (*63*).

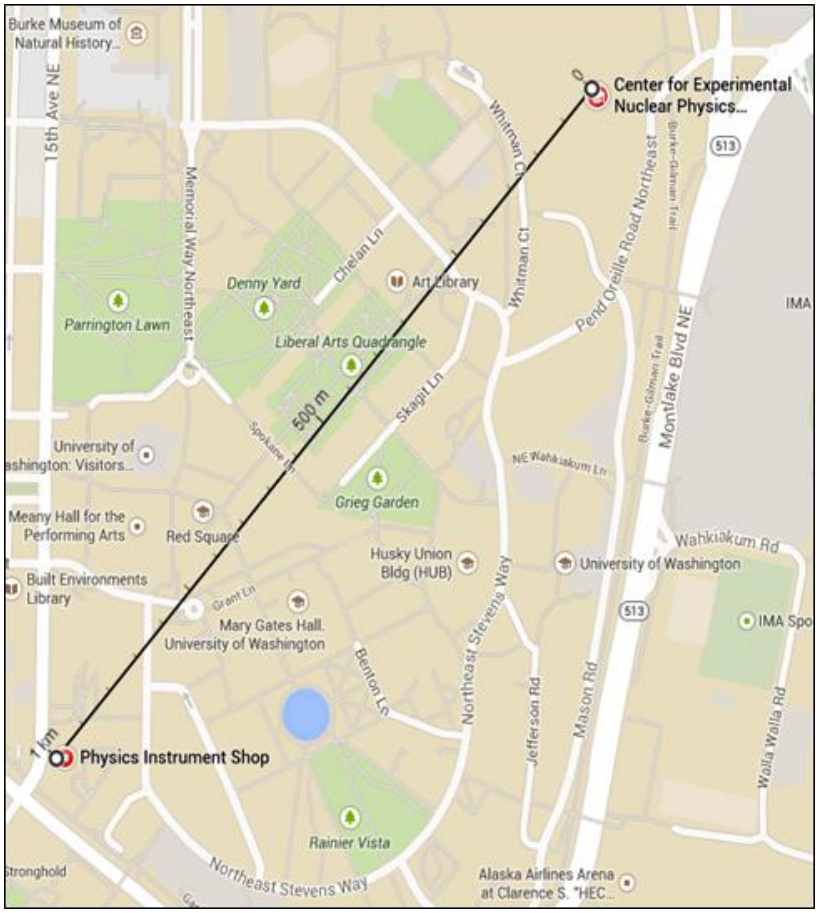

Figure 6.1 Proposal for setting up two trap systems at Physics Department and CENPA. The actual fiber length required is probably about 1.5 km.

We already built another parabolic mirror trap and are working toward remote ion-ion entanglement on a few meters distance. The major improvement of this new trap is we implemented two perpendicular piezoelectric motors at the side of needle electrode. The ion positioning is done by moving needle electrode in all three directions rather than varying DC

bias voltages in the old mirror trap. The advantage is that the micro-motion will be reduced and we expect to see the ion imaging close to diffraction limit, which also potentially improves the fiber coupling efficiency. In Chapter 5.2, we have an ion-photon entangled state through optical fiber coupling as:

$$|\psi\rangle = (|0\rangle_{ion}|\sigma^{+}\rangle_{pho} - |1\rangle_{ion}|\sigma^{-}\rangle_{pho})/\sqrt{2}. \quad (6.25)$$

If we have two identical system *a* and *b*, which generate two ion-photon pairs, their quantum state will become

$$(|0\rangle_a|+\rangle_a - |1\rangle_a|-\rangle_a)\otimes(|0\rangle_b|+\rangle_b - |1\rangle_b|-\rangle_b)/2 =$$
$$|0\rangle_a|+\rangle_a|0\rangle_b|+\rangle_b - |0\rangle_a|+\rangle_a|1\rangle_b|-\rangle_b - |1\rangle_a|-\rangle_a|0\rangle_b|+\rangle_b + |1\rangle_a|-\rangle_a|1\rangle_b|-\rangle_b/2. \quad (6.26)$$

Here I abbreviated $\sigma^{\pm}$ as ± for simplicity. Using the Bell state basis:

$$|\Phi^{\pm}\rangle = (|0\rangle_a|0\rangle_b \pm |1\rangle_a|1\rangle_b)/\sqrt{2}, \text{ and}$$
$$|\Psi^{\pm}\rangle = (|0\rangle_a|1\rangle_b \pm |1\rangle_a|0\rangle_b)/\sqrt{2}, \quad (6.27)$$

we can rewrite Eq. 6.27 as:

$$|\Phi^{+}\rangle_{ion}|\Phi^{+}\rangle_{pho} - |\Phi^{-}\rangle_{ion}|\Phi^{-}\rangle_{pho} - |\Psi^{+}\rangle_{ion}|\Psi^{+}\rangle_{pho} + |\Psi^{-}\rangle_{ion}|\Psi^{-}\rangle_{pho}. \quad (6.28)$$

We can generate two separate ion-photon pairs, and send both photons to a non-polarizing beam splitter followed by two PMTs. There are 4 possible situations when these two photons pass the splitter, as shown in Figure 6.2.

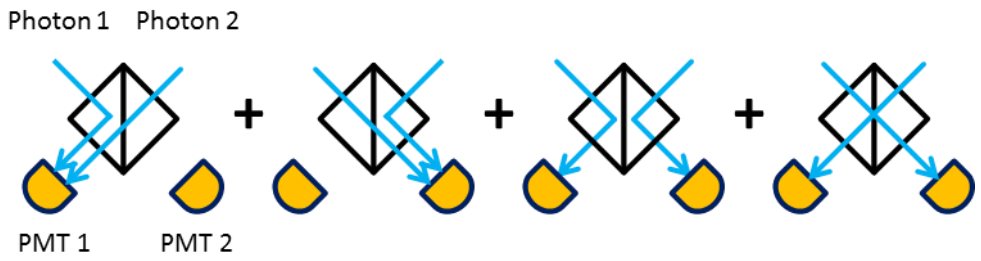

Figure 6.2. Four possible routes as two photons pass through a non-polarizing beam splitter. When a photon is reflected, it is subjected to a 90° phase shift. Therefore, the last two pathways destructively interfere for symmetric photon states, such as $|\Phi^{\pm}\rangle$ and $|\Psi^{+}\rangle$.

The last two possible routes in Figure 6.2 have opposite phase due to π phase shift of reflected photon, so they cancel each other for symmetric Bell's state of photon. Therefore, when both PMTs register a photon, the photon state will be the only anti-symmetric state in Eq. 6.28, which is the $|\Psi^{-}\rangle$ state, and the barium ions will be in the anti-symmetric Bell state:

$$|\Psi^{-}\rangle = (|0\rangle_a|1\rangle_b - |1\rangle_a|0\rangle_b)/\sqrt{2}. \tag{6.29}$$

We can then perform random state rotation of 0 or π radians for ion *a*, and π/4 or 3π/4 radians for ion *b*, and readout both ion states to test Bell's inequality violation. These angles are chosen to violate the Bell's inequality at the most extent. The measurement of two qubit states results in one of the four outcomes: ($|0\rangle_a|0\rangle_b$, $|0\rangle_a|1\rangle_b$, $|1\rangle_a|0\rangle_b$, $|1\rangle_a|1\rangle_b$), which are used to derive the correlation parameters in Eq. 3.18. This is a simple idea, but the true challenge is to close the two loopholes simultaneously. There are some technical problems to be addressed. First, how practical is wiring our specialized optical fiber for 1 km? We asked two companies for a quote of such a fiber, and they both can provide a single mode optical fiber about 1.5 km for about five thousand dollars. So such a fiber is available and not extremely expensive. Secondly, in order to observe the photon entanglement, the photon detection at both PMTs should be

indistinguishable, which means that the temporal and spatial overlapping of both photons at beam splitter should be no worse than 1 ns, which is about 30 cm (*5, 70*). It requires the synchronized excitation sources and fine control of the beam splitter placement. Another attractive solution is a fiber beam splitter, which guarantees perfect spatial overlap. One other important thing is the entanglement generation rate. The fiber we are interested in is HP460 from Thorlabs, and its attenuation rate is advertised as less than 30dB/km. Assuming it takes 1.5 km to connect Physics building and CENPA, attenuation would be approximately 31600. On average, our excitation rate is 20%, overall the fiber coupling efficiency of $\sigma^{\pm}$ emission is 2%, the PMT quantum efficiency is 20%, and optical component loss of 10%, and 25% of anti-symmetry Bell's state distribution, which leads to one entanglement detection in about twenty minutes. This number can be improved in many aspects, such as applying deformable mirror for fiber coupling or excitation rate improvement, which will both increase entanglement rate quadratically.

Last but not the least, the ion qubit state readout process needs to be done in fewer than 3 μs to close the locality loophole. The orthogonal measurement bases for the ion qubit states can be realized by ion qubit state rotation, followed by selective state shelving and cooling cycles described in Chapter 2.5. The ion qubit state is rotated by turning on the RF signal of the wire loops at the qubit resonant frequency. The impedance matching coil with amplified RF signal generates electromagnetic radiation, and rotates the ion state in a two qubit Bloch sphere. In our current setup, we can complete this process in around 5 μs. By further increasing the RF and the 1762 nm laser powers and focusing it more tightly, it is very reasonable to expect a 3 μs rotation/detection cycle. The Figure 6.3 shows the space-time diagram of the experimental procedure and the limiting factors of Bell's inequality violation test (*69*). Two identical setups, I

& II, are separated by 1 km and emit a photon at the same time, E_I & E_{II}. Each photon is coupled into an optical fiber and detected as event D_{PP}. Only when both PMTs register a photon, the ion qubit state rotation and readout is done. The angle of state rotations are randomly chosen at C_I & C_{II} after D_{PP} in order to prevent any post-selection probability. Another constraint is that the readout of ion qubits state, D_I & D_{II} must be finished before the light cone of C_I & C_{II} arrive to close the locality loophole, which is 3 μs for our proposal. One last consideration is the fidelity loss. For such a long optical fiber, due to the thermal and physical perturbations, lowers the purity of the state of polarization qubit. Thus, we may need to consider the frequency or time-bin qubit schemes, which are less vulnerable to fiber birefringence.

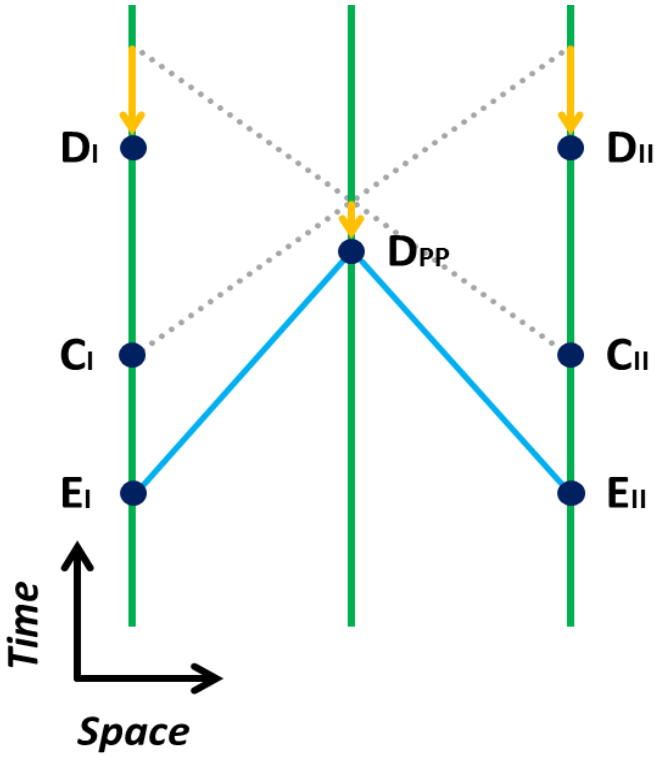

Figure 6.3. The spacetime diagram of events ordering for Bell's inequality violation test. E_I and E_{II} are the two events of photon emission. C_I and C_{II} are events of random detection basis generation. D_{PP} is where the two photons meet each other in a beam splitter. D_I and D_{II} are the ions state readout events.

In late 2015, there were three first-ever loophole-free Bell's inequality violation experiments published (*5-7*). Photons were used in all three experiments because of their mobility; they carry the entanglement information in different aspects. The first experiment from the Ronald Hanson's group in Delft University of Technology used the electron spin states of nitrogen vacancy (NV) centers in diamond as qubit state. Their entanglement scheme is similar to our proposal. First, two independent electron-photon entanglements pair are generated in time-bin scheme at separate locations 1.3 km apart. The two photons travel in two optical fibers to a third location in between, and collapse in an anti-symmetry Bell's state with 25% probability. As

a result, the two electron spin states are entangled remotely through entanglement swapping, and the NV center qubits' state detection is made by microwave rotation and selective cycling transition of the spin states. The main advantage of this protocol is the entanglement is established through the photons traveling in optical fibers, which can be extended over long distance. The second advantage is that the detection efficiency of electron spin states is close to unity. The disadvantage is the attenuation of optical fiber increases with distance, so the entanglement rate is as low as one pair per hour for about 1 km separation in their experiment. Also, the detection of electron state is usually of micro second scale, which compensates the long separation distance at the first place to close the locality loophole. Overall, this scheme sacrifices the entanglement rate in exchange for the separation between entangled pair and state readout efficiency.

The other two Bell's inequality violation experiments, one done by Anton Zeilinger's group in Universität Wien and the other by Sae Woo Nam's group in NIST, used spontaneous parametric down-conversion (SPDC) in the periodically poled potassium titanyl phosphate (PPKTP) crystal, which generates polarization entangled photon pairs (*71*, *72*). Each entangled photon is coupled into different optical fiber and travels to the detection site. The advantage is the entanglement generation rate is as high as ~10 KHz. The disadvantage of using a single photon as a qubit is the detection efficiency losses, which comes from the optical fiber coupling, fiber attenuation, and efficiency of the photon detector. This limits the separation of two measurements in order to close the detection loophole. The high entanglement generation rate is at the cost of short distance between entangled pair. Equipped with superconducting devices of ~90% single photon detection efficiency, the distance between two measurements is around 100 meters in both experiments.

These two different schemes provide the long-lived entangled electron pair over long distance or a rapid photon-photon entanglement generation, which are both realized through photon usage. The flexibility of photon application plays an important role in many quantum researches. From particle to wave to wave-particle duality, the way we see the photon evolves from classical physics to quantum mechanics, and we would like to continue this journey. In this thesis, I developed the parabolic mirror trap and increased the collection efficiency of the trapped ion's fluorescence. This setup generates entangled ion-photon pairs, and can improve the scalability of ion-photon qubit system.

BIBLIOGRAPHY

1. D. Hanneke *et al.*, New Measurement of the Electron Magnetic Moment and the Fine Structure Constant. *Physical Review Letters* **100**, 120801 (2008).

2. A. Einstein, Zur Elektrodynamik bewegter Körper. *Annalen der Physik* **322**, 891-921 (1905).

3. A. Einstein *et al.*, Can Quantum-Mechanical Description of Physical Reality Be Considered Complete? *Physical Review* **47**, 777 (1935).

4. J. S. Bell, On the einstein podolsky rosen paradox. *Physics* **1**, 195 (1964).

5. B. Hensen *et al.*, Loophole-free Bell inequality violation using electron spins separated by 1.3 kilometres. *Nature* **526**, 682-686 (2015).

6. M. Giustina *et al.*, Significant-Loophole-Free Test of Bell's Theorem with Entangled Photons. *Physical Review Letters* **115**, 250401 (2015).

7. L. K. Shalm *et al.*, Strong Loophole-Free Test of Local Realism. *Physical Review Letters* **115**, 250402 (2015).

8. M. A. Nielsen, I. L. Chuang, *Quantum Computation and Quantum Information: 10th Anniversary Edition*. (Cambridge University Press, 2011).

9. C. H. Bennett, G. Brassard, in *International Conference on Computers, Systems and Signal Processing*. (1984), vol. 175, pp. 8.

10. W. K. Wootters, W. H. Zurek, A single quantum cannot be cloned. *Nature* **299**, 802-803 (1982).

11. P. W. Shor, Polynomial-Time Algorithms for Prime Factorization and Discrete Logarithms on a Quantum Computer. *SIAM Journal on Computing* **26**, 1484-1509 (1997).

12. L. K. Grover, in *Proceedings of the twenty-eighth annual ACM symposium on Theory of computing*. (ACM, 1996), pp. 212-219.

13. I. M. Georgescu *et al.*, Quantum simulation. *Reviews of Modern Physics* **86**, 153 (2014).

14. C. A. Mack, Fifty Years of Moore's Law. *IEEE Transactions on Semiconductor Manufacturing* **24**, 202-207 (2011).

15. R. P. Feynman, Simulating Physics with Computers. *International Journal of Theoretical Physics* **21**, 467-488 (1982).

16. S. A. Cook, in *Proceedings of the third annual ACM symposium on Theory of computing*. (ACM, 1971), pp. 151-158.

17. S. Aaronson, The Limits of Quantum Computers. *Scientific American* **298**, 62-69 (2008).

18. K. D. Greve *et al.*, Quantum-dot spin-photon entanglement via frequency downconversion to telecom wavelength. *Nature* **491**, 421-425 (2012).

19. W. B. Gao, P. Fallahi, E. Togan, J. Miguel-Sanchez, A. Imamoglu, Observation of entanglement between a quantum dot spin and a single photon. *Nature* **491**, 426-430 (2012).

20. E. Togan *et al.*, Quantum entanglement between an optical photon and a solid-state spin qubit. *Nature* **466**, 730-734 (2010).

21. H. Bernien *et al.*, Two-Photon Quantum Interference from Separate Nitrogen Vacancy Centers in Diamond. *Physical Review Letters* **108**, 043604 (2012).

22. T. Wilk *et al.*, Entanglement of Two Individual Neutral Atoms Using Rydberg Blockade. *Physical Review Letters* **104**, 010502 (2010).

23. L. Li, Y. O. Dudin, A. Kuzmich, Entanglement between light and an optical atomic excitation. *Nature* **498**, 466-469 (2013).

24. C. Eichler *et al.*, Observation of Entanglement between Itinerant Microwave Photons and a Superconducting Qubit. *Physical Review Letters* **109**, 240501 (2012).

25. B. B. Blinov, D. L. Moehring, L.-M. Duan, C. Monroe, Observation of entanglement between a single trapped atom and a single photon. *Nature* **428**, 153-157 (2004).

26. A. Stute *et al.*, Tunable ion-photon entanglement in an optical cavity. *Nature* **485**, 482-485 (2012).

27. D. P. DiVincenzo, The Physical Implementation of Quantum Computation. *Fortschritte der Physik* **48**, 771-783 (2000).

28. S. Boixo *et al.*, Characterizing Quantum Supremacy in Near-Term Devices. *https://arxiv.org/abs/1608.00263v2*, (2016).

29. S. Debnath *et al.*, Demonstration of a small programmable quantum computer with atomic qubits. *Nature* **536**, 63-66 (2016).

30. E. Kawakami *et al.*, Gate fidelity and coherence of an electron spin in an Si/SiGe quantum dot with micromagnet. *Proc Natl Acad Sci U S A* **113**, 11738-11743 (2016).

31. V. Mourik *et al.*, Signatures of Majorana Fermions in Hybrid Superconductor-Semiconductor Nanowire Devices. *Science* **336**, 1003-1007 (2012).

32. M. Hirose, P. Cappellaro, Coherent feedback control of a single qubit in diamond. *Nature* **532**, 77-80 (2016).

33. G. Popkin, in *DOI: 10.1126/science.aal0442*. (Science, 2016).

34. C. Monroe, J. Kim, Scaling the Ion Trap Quantum Processor. *Science* **339**, 1164-1169 (2013).

35. C. Monroe *et al.*, Large-scale modular quantum-computer architecture with atomic memory and photonic interconnects. *Physical Review A* **89**, 022317 (2014).

36. A. V. Steele *et al.*, Photoionization and photoelectric loading of barium ion traps. *Physical Review A* **75**, 053404 (2007).

37. W. Paul, Electromagnetic traps for charged and neutral particles. *Reviews of Modern Physics* **62**, 531 (1990).

38. R. E. March, An Introduction to Quadrupole Ion Trap Mass Spectrometry. *Journal of Mass Spectrometry* **32**, 351-369 (1997).

39. D. Leibfried *et al.*, Quantum dynamics of single trapped ions. *Reviews of Modern Physics* **75**, 281 (2003).

40. C. J. Foot, *Atomic Physics*. (Oxford University Press, 2005).

41. J. J. Sakurai, *Modern Quantum Mechanics*. (Pearson Education, 2006).

42. D. D. Munshi *et al.*, Precision measurement of branching fractions of 138Ba+. *Physical Review A* **91**, 040501 (2015).

43. P. Andris, Matching and tuning RF coils for NMR tomograph. *Meas Sci Rev* **1**, 115-118 (2001).

44. J. F. Clauser *et al.*, Proposed Experiment to Test Local Hidden-Variable Theories. *Physical Review Letters* **23**, 880 (1969).

45. W. Gerlach, O. Stern, Der experimentelle Nachweis der Richtungsquantelung im Magnetfeld. *Zeitschrift für Physik* **9**, 349-352 (1922).

46. J. S. Bell, *Speakable and Unspeakable in Quantum Mechanics*. (Cambridge University Press, 1987).

47. S. J. Freedman, J. F. Clauser, Experimental Test of Local Hidden-Variable Theories. *Physical Review Letters* **28**, 938 (1972).

48. A. Aspect *et al.*, Experimental Test of Bell's Inequalities Using Time-Varying Analyzers. *Physical Review Letters* **49**, 1804 (1982).

49. M. A. Rowe *et al.*, Experimental violation of a Bell's inequality with efficient detection. *Nature* **409**, 791-794 (2001).

50. P. M. Pearle, Hidden-Variable Example Based upon Data Rejection. *Physical Review D* **2**, 1418 (1970).

51. A. Reiserer, N. Kalb, G. Rempe, S. Ritter, A quantum gate between a flying optical photon and a single trapped atom. *Nature* **508**, 237-240 (2014).

52. C. Cabrillo *et al.*, Creation of entangled states of distant atoms by interference. *Physical Review A* **59**, 1025 (1999).

53. C. Auchter, C. K. Chou, T. W. Noel, B. B. Blinov, Ion–photon entanglement and Bell inequality violation with 138Ba+. *JOSA B* **31**, 1568-1572 (2014).

54. D. L. Moehring *et al.*, Entanglement of single-atom quantum bits at a distance. *Nature* **449**, 68-71 (2007).

55. J. Brendel *et al.*, Pulsed Energy-Time Entangled Twin-Photon Source for Quantum Communication. *Physical Review Letters* **82**, 2594 (1999).

56. S. D. Barrett, P. Kok, Efficient high-fidelity quantum computation using matter qubits and linear optics. *Physical Review A* **71**, 060310 (2005).

57. D. J. Berkeland, J. D. Miller, J. C. Bergquist, W. M. Itano, D. J. Wineland, Minimization of ion micromotion in a Paul trap. *Journal of Applied Physics* **83**, 5025 (1998).

58. R. Maiwald *et al.*, Stylus ion trap for enhanced access and sensing. *Nature Physics* **5**, 551-554 (2009).

59. J. D. Sterk *et al.*, Photon collection from a trapped ion-cavity system. *Physical Review A* **85**, 062308 (2012).

60. D. Stick *et al.*, Ion trap in a semiconductor chip. *Nature Physics* **2**, 36-39 (2005).

61. G. Shu, C. K. Chou, N. Kurz, M. R. Dietrich, B. B. Blinov, Efficient fluorescence collection and ion imaging with the “tack” ion trap. *JOSA B* **28**, 2865-2870 (2011).

62. R. Maiwald *et al.*, Collecting more than half the fluorescence photons from a single ion. *Physical Review A* **86**, 043431 (2012).

63. D. Hucul *et al.*, Modular entanglement of atomic qubits using photons and phonons. *Nature Physics* **11**, 37-42 (2014).

64. L. Zhu, P.-C. Sun, D.-U. Bartsch, W. R. Freeman, Y. Fainman, Wave-front generation of Zernike polynomial modes with a micromachined membrane deformable mirror. *Applied Optics* **38**, 6019-6026 (1999).

65. T. F. Gloger *et al.*, Ion-trajectory analysis for micromotion minimization and the measurement of small forces. *Physical Review A* **92**, 043421 (2015).

66. N. Kurz *et al.*, Measurement of the branching ratio in the 6P3/2 decay of Ba II with a single trapped ion. *Physical Review A* **77**, 060501 (2008).

67. L. Luo *et al.*, Protocols and techniques for a scalable atom–photon quantum network. *Fortschritte der Physik* **57**, 1133-1152 (2009).

68. R. C. Jones, A New Calculus for the Treatment of Optical SystemsI. Description and Discussion of the Calculus. *JOSA* **31**, 488-493 (1941).

69. C. Simon *et al.*, Robust Long-Distance Entanglement and a Loophole-Free Bell Test with Ions and Photons. *Physical Review Letters* **91**, 110405 (2003).

70. C. K. Hong *et al.*, Measurement of subpicosecond time intervals between two photons by interference. *Physical Review Letters* **59**, 2044 (1987).

71. A. Fedrizzi, A. Poppe, A. Zeilinger, T. Herbst, T. Jennewein, A wavelength-tunable fiber-coupled source of narrowband entangled photons. *Optics Express* **15**, 15377-15386 (2007).

72. P. B. Dixon *et al.*, Heralding efficiency and correlated-mode coupling of near-IR fiber-coupled photon pairs. *Physical Review A* **90**, 043804 (2014).

VITA

Chen-Kuan Chou was born on February 1st, 1983 in Taipei, Taiwan. He attended the National Taiwan University, graduating with a B.S. degree in Physics in 2005 and a M.S. degree in Physics in 2007. His master's research was about physical modeling of fibrous tissue with nonlinear laser microscopy. After that, he started mandatory military service in the Taiwan Army for one year and worked as a research assistant in NTU for another year. In 2009, he joined the University of Washington as a graduate student in the Physics Department, and joined Boris Blinov's trapped ion quantum computing group in 2010. He built a novel ion trap and generated ion-photon entanglement with it. In 2017, he graduated, and his journey continues!